

Thermal structure of the upper atmosphere of Venus simulated by a ground-to-thermosphere GCM



G. Gilli^{a,*}, S. Lebonnois^a, F. González-Galindo^b, M.A. López-Valverde^b, A. Stolzenbach^c,
F. Lefèvre^c, J.Y. Chaufray^c, F. Lott^a

^aLaboratoire de Météorologie Dynamique (LMD)/IPSL, CNES, CNRS, Paris, France

^bInstituto de Astrofísica de Andalucía (IAA), CSIC, Granada, Spain

^cLaboratoire Atmospheres, Milieux, Observations Spatiales (LATMOS), IPSL, Paris, France

ARTICLE INFO

Article history:

Available online 15 September 2016

ABSTRACT

We present here the thermal structure of the upper atmosphere of Venus predicted by a full self-consistent Venus General Circulation Model (VGCM) developed at *Laboratoire de Météorologie Dynamique* (LMD) and extended up to the thermosphere of the planet. Physical and photochemical processes relevant at those altitudes, plus a non-orographic GW parameterisation, have been added. All those improvements make the LMD-VGCM the only existing ground-to-thermosphere 3D model for Venus: a unique tool to investigate the atmosphere of Venus and to support the exploration of the planet by remote sounding. The aim of this paper is to present the model reference results, to describe the role of radiative, photochemical and dynamical effects in the observed thermal structure in the upper mesosphere/lower thermosphere of the planet. The predicted thermal structure shows a succession of warm and cold layers, as recently observed. A cooling trend with increasing latitudes is found during daytime at all altitudes, while at nighttime the trend is inverse above about 110 km, with an atmosphere up to 15 K warmer towards the pole. The latitudinal variation is even smaller at the terminator, in agreement with observations. Below about 110 km, a nighttime warm layer whose intensity decreases with increasing latitudes is predicted by our GCM. A comparison of model results with a selection of recent measurements shows an overall good agreement in terms of trends and order of magnitude. Significant data-model discrepancies may be also discerned. Among them, thermospheric temperatures are about 40–50 K colder and up to 30 K warmer than measured at terminator and at nighttime, respectively. The altitude layer of the predicted mesospheric local maximum (between 100 and 120 km) is also higher than observed. Possible interpretations are discussed and several sensitivity tests performed to understand the data-model discrepancies and to propose future model improvements.

© 2016 Elsevier Inc. All rights reserved.

1. Introduction

The recent exploration by the Venus Express (VEx) orbiter and the increasing number of ground based observations noticeably improved the knowledge of our neighbouring planet. Prior to VEx, satellite and ground-based observations of the upper mesosphere and thermosphere of the planet (90–180 km) were both limited in spatial and temporal coverage. Measurements by Pioneer Venus (PV), both mass spectrometer and drag observations down to 140 km (Niemann et al., 1980), together with accelerometer data below 130 km (Keating et al., 1985; Seiff, 1983), provided data on the composition and structure of the Venus ther-

mosphere for the first time. This enabled the construction of a 1-D semi-empirical model of temperature and composition, the VTS3 by Hedin et al. (1983), mainly based on PV measurements above 140 km and on model extrapolations assuming hydrostatic equilibrium between 100–140 km.

After eight years in orbit (2006–2014), exceeding its planned life, VEx collected a considerable amount of data from several instruments on board (Svedhem et al., 2015). Also, aerobraking manoeuvres carried the spacecraft down to 130 km altitude at the end of the mission (Svedhem and Müller-Wodarg, 2014), provided direct measurements of local atmospheric densities and temperature of a region difficult to sound (130–160 km). The short and long-term density variability observed at those altitudes is surprisingly higher than expected and represents a challenge to current theoretical models. All those new measurements revealed a dy-

* Corresponding author.

E-mail address: ggilli@lmd.jussieu.fr (G. Gilli).

namically active upper atmosphere, much more complex than predicted by VTS3. The interaction between lower and upper regions and gravity wave propagation (Altieri et al., 2014; Zaluza et al., 2013) have to be taken into account to interpret the observed results.

Temperature values have been successfully retrieved by several instruments on board VEX. The radio occultation measurement by VeRa (Venus Radio Science experiment) provided high vertical resolution pressure and temperature profiles in the altitude range 40–90 km (Tellmann et al., 2009). Strong IR absorption bands of CO₂ at 4.3 μm observed by VIRTIS (Visible and InfraRed Thermal Imaging Spectrometer) between 65 and 96 km altitudes have been used to retrieve nighttime temperature and aerosol altitude profiles in the mesosphere (Grassi et al., 2010; 2014; Haus et al., 2013, 2014; Migliorini et al., 2012). In addition, ground based observations provide higher spectral resolution and a better spatial coverage which complement satellite observations: sub-millimeter observations of CO lines from Earth constrain on the thermal structure between approximately 70 and 110 km (Clancy et al., 2012). Kinetic temperature can also be calculated at about 110 km from the width of narrow CO₂ emission lines using infrared heterodyne spectroscopy (Sonnabend et al., 2010). Those results showed that the thermal structure of the Venus mesosphere varies strongly with latitude: polar regions were surprisingly observed up to 20 K warmer than equatorial latitudes at most pressure levels between the cloud tops and 100 km. They also confirmed the presence of a colder region (the so called “cold collar”) around 65°–70°S latitude, at about 10² Pa (65 km altitude approximately).

The upper mesosphere/lower thermosphere was sounded by solar/stellar occultation experiments at the terminator and nighttime by SOIR/VEX (Mahieux et al., 2015) and SPICAV/VEX (Piccialli et al., 2015), respectively. They show a complex thermal structure above 90 km with a large vertical and spatial variability, still not fully explained by current models (Bougher et al., 2015). At the terminator, the observed temperature profiles are characterised by a local maximum around 105 km, that was interpreted by Bougher et al. (2015) to be produced by solar absorption in the CO₂ IR bands during daytime and then advected to the terminator. Above, a cold layer around 125–130 km is observed, which Bougher et al. (2015) suggested to be caused by CO₂ 15 μm cooling.

Above 130 km the observed thermal structure shows features of the extreme EUV absorption, with increasing temperatures above 140–150 km. At night, a warm region possibly resulting from subsidence of day-to-night air circulation was observed by SPICAV in the altitude range 90–100 km. On the dayside, temperatures from 100 to 150 km have been retrieved using infrared CO non-LTE emission at 4.7 μm by VIRTIS-H (Gilli et al., 2015). A hint of local maximum (230 ± 40 K) around 115 km near the terminator at equatorial latitudes is observed, although with large uncertainties. However, at noon in the equatorial regions, those retrieval results show lower temperatures than expected by previous models (Brecht et al., 2012) and in contrast to an upper mesosphere in pure radiative balance. In addition to this, nadir measurements of non-LTE CO₂ emissions at 4.3 μm by VIRTIS-H on board VEX have been used to retrieve daytime temperature in a wide altitude range, between 10 and 10⁻³ Pa (100–140 km, approximately) by Peralta et al. (2016). They show a maximum of 195 ± 10 K in the sub-solar region decreasing with latitude and local time, in agreement with Brecht et al. (2012). These nadir non-LTE measurement also show a “plateau” between 30°S and 30°N, not predicted by global circulation models. Daytime thermosphere temperatures have been also inferred from a few CO₂ UV dayglow observations by SPICAV (Chaufray et al., 2012). These authors estimated the temperature near 145 km at 290 ± 60 K, comparable with noon temperatures predicted by the VTS3 model by Hedin et al. (1983).

In the last decade the scientific community has conducted several studies to carry out a systematic and exhaustive inter-comparison and validation of both satellite and ground-based telescope measurements after the arrival of VEX, taking also into account the geometry of observations and the different retrieval techniques. Those efforts have been accomplished within the context of several international projects (e.g the scientific Team supported by the International Space Science Institute (ISSI), Bern, Switzerland (Limaye et al., 2015)) and they contribute an unprecedented insight into the complex dynamical mechanisms occurring in the atmosphere of our sister planet. Nevertheless, VEX results also raised new challenging questions to be answered. Sophisticated climate models and synergies with the data analysis are fundamental to interpret the observed results and to help build a consistent picture of the spatial and temporal evolution of Venus atmosphere. Unfortunately, too many free parameters and theoretical uncertainties (i.e limited gravity wave constraints for wave breaking, quenching rate coefficient for the IR mesospheric cooling, etc) prevent existing GCMs to use a unique set of wind fields, eddy diffusion coefficients and wave drag parameters to reproduce observed density, temperature and airglow variations (Bougher et al., 2006).

A 3D Thermospheric General Circulation Model (TGCM) for Venus with coupled energetics, dynamics and composition described in Bougher et al. (1988) was recently updated to address the key VEX observations in the altitude range between 70 and 200 km, in particular to reproduce the observations of the various airglow distributions (Brecht et al., 2011), dayside temperatures (Brecht and Bougher, 2012) and temperatures at the terminator (Bougher et al., 2015).

In this paper we present an improved version of the LMD Venus GCM (Lebonnois et al., 2012, 2010), now extended up to approximately 150 km. We aim here at exploring the mechanisms at work from 90 to 150 km altitudes, focusing mainly on the thermal structure. The inclusion of the main processes contributing to the thermal balance of the upper atmosphere of Venus (i.e IR heating by CO₂, IR CO₂ 15 μm cooling, extreme UV heating, thermal conduction) and the coupling with a photochemical model (Stolzenbach et al., 2014), provide a fully self-consistent and quantitative description of the Venusian atmosphere. Those improvements make the LMD-GCM the only existing ground-to-thermosphere 3D model. In addition, a non-orographic gravity waves parameterisation following Lott and Guez (2013) is included in the LMD Venus GCM for the first time.

Section 2 describes the model and the physical processes implemented in this version. The results of the reference simulation, in terms of thermal balance and thermal structure variation are presented in the Section 3, with additional details on the composition given in Section 6. Comparison to observational data by Venus Express mission and ground based telescopes is done in Section 4. Section 5 discusses the sensitivity of the thermal structure to key model parameters, then conclusions are given in Section 7.

2. LMD-VGCM: model description and improvements

The Venus GCM developed at Laboratoire de Meteorologie Dynamique (Lebonnois et al., 2010), hereinafter LMD-VGCM, is based on the tools and experience gathered for the GCMs of the Earth’s atmosphere (Hourdin et al., 2006) and Mars atmosphere (Forget et al., 1999). The dynamical core is a common part for the three terrestrial planets, while the physical core is specific for the conditions and characteristics of each planet. The model solves the primitive equations of hydrodynamics in a sphere, using a finite difference discretisation scheme which conserves both potential enstrophy for barotropic non divergent flows, and total angular momentum for axisymmetric flow. In the top four lay-

Table 1

List of chemical species included in the model. List of chemical species included in the model. (l) stands for liquid phase, (g) for gas phase.

1	CO ₂	11	H	21	CICO ₃	31	H ₂ O _(l)
2	CO	12	OH	22	COCl ₂	32	S ₂
3	H ₂	13	HO ₂	23	S	33	ClSO ₂
4	H ₂ O _(g)	14	H ₂ O ₂	24	SO	34	OSCl
5	H ₂ O _(l)	15	Cl	25	SO ₂		
6	O(¹ D)	16	ClO	26	SO ₃		
7	O	17	Cl ₂	27	S ₂ O ₂		
8	O ₂	18	HCl	28	OCS		
9	O ₂ (¹ Δg)	19	HOCl	29	HSO ₃		
10	O ₃	20	CICO	30	H ₂ SO ₄ (g)		

ers of the GCM a sponge layer is included, with Rayleigh friction to relax the horizontal winds and potential energy to the mean zonal values. The Rayleigh friction is not used here as a general drag for the upper atmosphere. In the atmosphere of Venus the conservation of angular momentum is an important issue. In the configuration used in the LMD-VGCM the conservation of angular momentum is quite good, with numerical residuals around 10% of the amplitude of the surface physical forcings, as described in Lebonnois et al. (2012). Compared to Lebonnois et al. (2010) (hereinafter L10), the main change in the physical parameterisation of the lower atmosphere is the planetary boundary layer scheme. The vertical eddy diffusion coefficient and the time evolution of the mixed variables are now computed following the Mellor and Yamada (1982) scheme, used also for the other planetary GCMs developed at LMD (Earth, Mars and Titan), and described in the Appendix B of Hourdin et al. (2002). The time step is about 1.5 min, as in (Lebonnois et al., 2010). Concerning the radiative transfer below 100 km, the heating rates for the short-wave radiation are taken from look-up tables based on the work by Crisp (1986). Then the rates are interpolated for the correct solar zenith angle for each GCM grid point, to include the diurnal cycle. For the long-wave radiation a radiative transfer code based on net exchange rate matrices is used, following the formalism developed by Eymet et al. (2009). This version of the LMD Venus GCM was previously used to compute self-consistently the thermal structure of the atmosphere of Venus and to interpret VEx observations around the cloud tops (Grassi et al., 2014; Migliorini et al., 2012). However, the complex and dynamically active upper regions unveiled by VEx demanded modelling efforts to include dominant radiative and chemical processes above about 100 km. Moreover, several modelling improvements have been done in the last 5 years for the LMD-VGCM. For instance, new physical packages are under development: a microphysical model dedicated to study the cloud system by Määttänen et al. (2015), Guilbon et al. (2015) and a mesoscale module (Lefevre et al., 2016 (submitted)) (both not included in this version of the VGCM). In this section we describe the model improvements focused on the vertical extension of the LMD-VGCM up to the lower thermosphere (up to 150 km approximately).

2.1. Vertical extension

The first step required for the vertical extension was to add pressure levels to the previous version of the VGCM based on 50 hybrid coordinates (i.e. $p = a_p + b_p p_s$ with p_s the surface pressure and a_p and b_p listed in Table 1, L10). A total of 28 pressure levels were added in order to reach thermospheric altitudes of about 150 km. They have been calculated through the hydrostatic equation, $P(z_2) = P(z_1) \exp(-\frac{z_2 - z_1}{H})$, with $z_1 < z_2$, where H is the scale height $H = RT/gM$, R the perfect gas constant ($R = 8.32 \text{ J mol}^{-1} \text{ K}^{-1}$), g the gravitational constant ($g = 8.87 \text{ m s}^{-2}$) and M the mean molecular mass for Venus ($M = 43.55 \text{ g/mol}$). Note that M is

explicitly calculated in the physics of the model. The vertical sampling is approximately 2–3 km between 100 and 150 km. The final grid consists of 78 vertical levels and a horizontal resolution of 48 longitudes \times 32 latitudes ($7.5^\circ \times 5.625^\circ$).

The following step was to include into the GCM the physical processes relevant to the upper atmosphere. At the low gas densities typical of upper atmospheric regions the impact of non-LTE effects is well known by a number of theoretical models of terrestrial planet atmospheres (Fox and Bougher, 1991; Keating et al., 1980; López-Puertas and Taylor, 2001). In these non-LTE models there are normally two separate terms of importance at thermospheric altitudes which require specific treatment, the IR cooling by CO₂ at 15 μm and the solar heating by CO₂ in its near-IR bands (1–5 μm). However, a comprehensive on-line implementation of a complex non-LTE model into a GCM is not straightforward and proper simplifications are required. The strategy adopted in this work was to follow the parameterisations already developed for the LMD Mars GCM, computationally compatible with 3D GCM simulations. The Martian GCM is a valuable precursor for the Venus GCM since both planets share many radiative and chemical processes related to CO₂ atmospheres. The heating and cooling rates due to the radiative transfer in gaseous CO₂ atmospheres at LTE and non-LTE conditions are calculated in both GCMs with separate parameterisations (see next sections for non-LTE parameterisation description). To combine the radiative tendencies in the transition region between the LTE and non-LTE regimes, the profiles of heating/cooling rates are smoothly merged as it follows:

$$Q = \alpha Q_{\text{NLTE}} + (1 - \alpha) Q_{\text{LTE}}$$

with $\alpha = 1/(1 + \frac{p}{p_{\text{merge}}})^4$. Taking into account that on Venus the non-LTE effects dominate above about 0.01 Pa (Gilli et al., 2009; López-Valverde et al., 2011; Roldán et al., 2000), this transition region is centered below that level. For the thermal cooling, p_{merge} has been fixed to 0.5 Pa. On another hand, for the solar heating we first verified a good match between the two radiative tendencies ($\frac{Q_{\text{LTE}}}{Q_{\text{NLTE}}} = 1$) below about 10 Pa, and then we fixed $p_{\text{merge}} = 10^2 \text{ Pa}$ to get a soft transition.

Above pressure 0.01 Pa (about 120 km altitude), the tendencies calculated by the GCM are purely a sum of non-LTE contributions. The processes implemented in the vertical extension are described in detail below and the heating/cooling rates calculated by the model are shown in Figs. 1 and 2.

2.2. NIR solar heating rate

The absorption of solar radiation in the CO₂ IR bands has a considerable impact on the thermal structure of Venus atmosphere above 90–100 km. Detailed calculations performed by a full non-LTE model (Roldán et al., 2000, hereinafter RO2000) showed that the net solar radiation absorption depends mainly on the density of the atmosphere, and to a smaller degree on the solar zenith angle, thermal structure and atomic oxygen abundance. This assumption permits tabulation of correction factors to convert LTE radiative transfer calculation rates into realistic non-LTE heating rates. This tabulation was done for the Mars' atmosphere by López-Valverde and López-Puertas (1994), and it allowed to calculate the heating rate in the Martian GCM using a 1-parameter formula (Eq. 1) that mimics the heating rates calculated by line-by-line non-LTE simulations, as shown in Forget et al. (1999) and González-Galindo et al. (2009). The essential aspects of the non-LTE 1D modelling are similar on Mars and Venus (Gilli et al., 2011; López-Valverde et al., 2011): this analogy enables to implement a similar non-LTE parameterisation on both planets. We assume the orbit of Venus circular $r = r_0$ with a mean Venus-Sun distance $r_0 = 0.72 \text{ AU}$, the axis perpendicular to the ecliptic plane, and no seasonal variation. At a pressure p , the solar heating is computed by

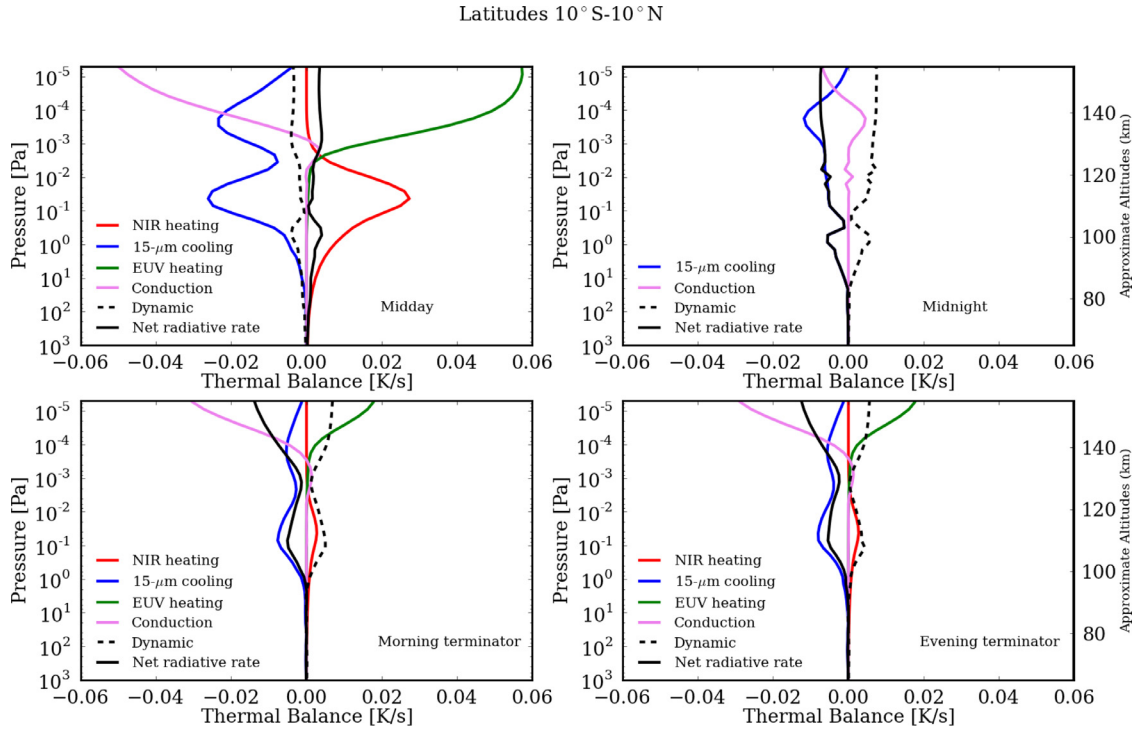


Fig. 1. Heating and cooling rates [K/s] of the reference simulation (after 10 Venus days) by the Venus LMD-GCM in the equatorial region (10°S–10°N): at midday, midnight, morning and evening terminators, as indicated. Approximate altitudes axis is showed on the right panels, as reference.

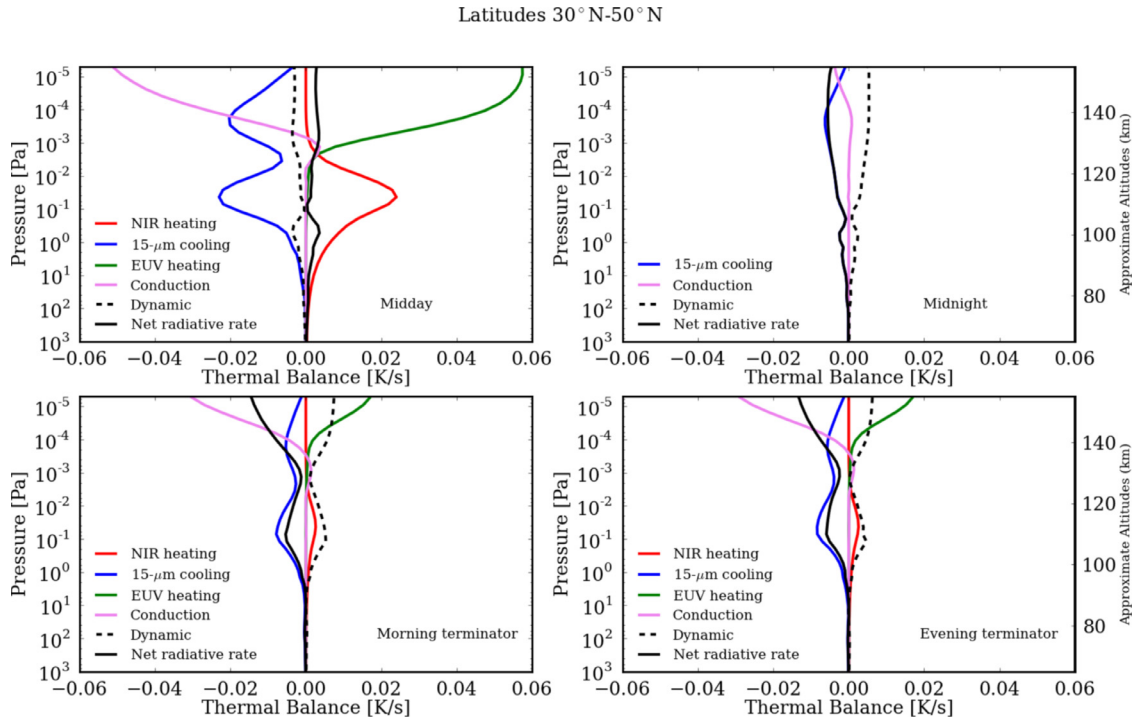


Fig. 2. As in Fig. 1 but for mid-latitude regions (30°N–50°N).

the following function:

$$\frac{\partial T}{\partial t}(p, r, \mu) = \frac{\partial T}{\partial t}(p_0, r_0, 0) \times \frac{r_0^2}{r^2} \sqrt{\frac{p_0}{p}} \tilde{\mu} \left(1 + \frac{p_1}{p}\right)^{-b} \quad (1)$$

where at a pressure $p_0 = 1320$ Pa and zero solar zenith angle $\mu = 0$ the heating rate per Venusian day (Vd) is $\frac{\partial T}{\partial t}(p_0, r_0, 0) = 18.13$ K/Vd (following precomputed tables for the solar flux and heat-

ing for Venus by Crisp (1986), p_1 is the approximate pressure below which non-LTE effects are significant ($p_1 = 0.008$ Pa), and $b = 1.362$. The cosine of the solar zenith angle corrected for atmospheric refraction is $\tilde{\mu} = [(1224\mu^2 + 1)/1225]^{1/2}$. Several tests were performed to fine-tune those parameters in order to reproduce the essentials of RO2000. It had to be considered that the relative abundance of atomic oxygen is variable in the GCM, while

it was fixed to VTS3 values in RO2000. Also, in the fine-tuning process particular attention was paid to get a good match in the lower mesosphere (in LTE conditions) with the VGCM solar heating rates based on Crisp (1986).

2.3. Thermal infrared

The thermal cooling by the CO₂ bands at 15 μm plays a key role to maintain the observed temperature structure and to moderate solar EUV flux changes during the solar cycle. Comprehensive studies of LTE breakdown of the main CO₂ levels helped explaining the long-standing problem of the cold lower thermosphere of the planet observed by Pioneer Venus (Schubert et al., 1980) between 10⁻² and 10⁻⁴ Pa and the small amplitude of its temperature variation during the 11-year solar cycle (Bougher et al., 1997; Sharma and Wintersteiner, 1990). The collisions with atomic oxygen are especially effective in exciting the vibrational levels of CO₂ molecules, thus enhancing the cooling at thermospheric heights where non-LTE prevails. The effectiveness of this enhancement process depends upon both the relative O density at a given pressure and the CO₂-O quenching rate coefficient k_{v-t} . On both Mars and Venus the collision of atomic oxygen with CO₂ molecules produces vibrationally excited CO₂ (O + CO₂ → CO₂* + O) which decays and radiates 15 μm photons through an optically thin path to space, thus cooling the atmosphere. Both quantities ([O] and k_{v-t}) are not very well known in the Venus atmosphere.

Regarding the [O] abundance, our knowledge is based only on nighttime mass spectrometer measurements down to ~135 km by ONMS/Pioneer Venus (for solar mean condition) (Kasprzak et al., 1993; Niemann et al., 1980) and indirect observation of the O₂ night-glow by VIRTIS/Venus Express (Gérard et al., 2013; Soret et al., 2014). No daytime measurements are available in the lower thermosphere of Venus, since PVO measurements were limited to altitudes above ~150 km. In this work, the atomic oxygen mixing ratio is calculated on-line by a coupled photochemical scheme (described in Section 2.7). Atomic oxygen is also vertically diffused and transported by the general circulation.

Laboratory and atmospheric measurements on the Earth indicate values for k_{v-t} between 1×10^{-12} cm³ s⁻¹ and 6×10^{-12} cm³ s⁻¹. This uncertainty is still an open and important question for planetary atmosphere studies (Feofilov and Kutepov, 2012; Huestis et al., 2008; Sharma, 2014). The CO₂-O deactivation rate (k_{v-t}) used here is a “median” value commonly used in terrestrial atmosphere models (3×10^{-12} cm³ s⁻¹) (e.g. Bougher et al., 2015; González-Galindo et al., 2013; Brecht et al., 2011). We followed the same strategy developed for the LMD-MGCM (González-Galindo et al., 2013). Our simplified non-LTE model takes into account the 5 strongest ro-vibrational bands of CO₂ (instead of 92 for the complete non-LTE model) and allows for a variable abundance of atomic oxygen.

2.4. EUV heating

Extreme UV (EUV) absorption is also parameterised following the scheme developed for the Mars GCM, described in González-Galindo et al. (2013, 2009, 2005) (hereinafter FGG2005). Fundamentally, the heating rates are obtained using pre-calculated photo-absorption coefficients. These coefficients, integrated in 36 spectral subintervals of varying spectral width in the 1–800 nm spectral range, were tabulated as a function of the column amount. From this tabulation, the total photo-absorption coefficients for each species are calculated by interpolation to the actual column amount and by a sum over the 36 spectral intervals. The abundance of the chemical species used in this parameterisation is self-consistently calculated in the VGCM through the coupled photochemical model.

This implementation is suitable for the VGCM since both Martian and Venusian thermospheres are dominated by CO₂ and its dissociation products O and CO, as well as N₂ and O₂. N₂ is not yet included in the photochemical scheme used here: the N₂ volume mixing ratio is fixed at 3.5 % below the homopause. We take into account the absorption of solar radiation by the most abundant species (CO₂, CO, O and O₂, and N₂). To include the variation of the UV solar flux with the 11-year solar cycle, we also followed the previous calculations by FGG2005 which reproduce the solar cycle 22 and 23 by a sinusoidal fit, and corrected it to Venus-Sun distance. The first year (2006) and the last year (2014) of the VEx mission are close to the minimum and the maximum of the solar cycle 24, respectively. In order to compare consistently our results with VEx measurements taken during those 8 years of the mission, we chose a solar flux value representative of “mean” solar conditions.

The EUV efficiency is another uncertain parameter in the modelling of terrestrial planets (Huestis et al., 2008). It is customary to adopt a nominal value and test for uncertainty range around that value. The range used in this work is [16–28 %], in agreement with detailed on-line calculations provided by Fox (1988), and compatible with acceptable 15 μm cooling rate k_{v-t} parameters.

2.5. Thermal conduction and molecular viscosity

The thermal conduction is one the main cooling mechanisms that, together with the CO₂ 15 μm cooling, balances the UV heating in the thermosphere of Venus. This process is governed by the following equation:

$$\frac{\partial T}{\partial t} = \frac{1}{\rho c_p} \frac{\partial}{\partial z} \left(k \frac{\partial T}{\partial z} \right) \quad (2)$$

where T is the temperature (K), ρ the density (kg/m³), c_p the specific heat and $k = AT^{0.69}$ is the thermal conduction coefficient (J m⁻¹ s⁻¹ K⁻¹), with a number density weighted average of the individual thermal conductivities.

A similar expression is used for the molecular viscosity, whose effect is to smooth velocity gradients as given below:

$$\frac{\partial S}{\partial t} = \frac{1}{\rho} \frac{\partial}{\partial z} \left(\mu \frac{\partial S}{\partial z} \right) \quad (3)$$

where S stands for the component of the horizontal wind (m s⁻¹) and μ is the coefficient of molecular viscosity (kg m⁻¹ s⁻¹) that is related to the thermal conduction coefficient by $k = \frac{1}{4}[9c_p - 5(c_p - R)]\mu$.

Here we followed the same implicit numerical scheme as described in Forget et al. (1999), in which both equations are discretised, allowing for longer and more stable time stepping.

2.6. Molecular diffusion

The thermosphere is also characterised by a transition region called the homopause, below which atomic and molecular constituents are well mixed by winds and turbulence, and above which the individual species begin to diffusively separate according to their individual masses or scale heights. Above that region the molecular diffusion dominates the vertical distribution of different species, leading the lightest atomic species (CO, O, He, H) to prevail up to the base of the exosphere.

In our model we use the algorithm developed by Chaufray et al. (2015) which describes the behaviour of chemical species by assuming that the diffusion velocity of each species is independent of the other species' diffusion velocity. The diffusive equilibrium condition is assumed at the upper boundary. The same procedure was previously implemented in the LMD-MGCM (see González-Galindo et al., 2013, for further details).

2.7. Photochemical model

The version of LMD-VGCM presented in this work includes a full photochemical model of the Venus atmosphere (Stolzenbach et al., 2015) which is based on the heritage of the Mars photochemical model (Lefèvre et al., 2008, 2004). It provides a comprehensive description of the chemistry of carbon dioxide, oxygen, hydrogen, chlorine and sulfur compounds. The chemical module includes 34 species, listed in Table 1, which interact through 19 photodissociation and 102 chemical reactions. The photodissociation rates are calculated with a modified version of Tropospheric Ultraviolet and Visible (TUV) model (Madronich and Flocke, 1999) that takes into account the solar zenith angle, the overhead column of CO₂ and SO₂ and the light scattering by Venusian aerosols to calculate the photodissociation rates. The optical depth from the clouds used is taken from Crisp (1986). The chemical reaction rates are taken from the compilation of kinetics data by Sander et al. (2011). The chemical model includes a parametrised cloud representation based on a fixed multimodal droplet radius size distribution (Knollenberg and Hunten, 1980). The cloud module also calculates at each physical time step the composition of the binary droplets of H₂SO₄/H₂O as well as the sedimentation rate of the condensed species, which is a function of aerosol size.

This 3D photochemical model is able to reproduce key observations like the strong H₂O and SO₂ decrease in the cloud region (Encrenaz et al., 2016). The implementation of a photochemical model in the LMD-VGCM enables the study of the horizontal distribution and vertical transport of chemical species for the first time up to 150 km.

2.8. Gravity waves parameterisation: motivation and preliminary implementation

The role of gravity wave (GW) propagation on the perturbation of density, temperature and cloud structure of the Venus atmosphere is commonly invoked in the literature to explain the observed variations. Gravity wave activity in Venus middle atmosphere is confirmed by several measurements, although their source is still unknown. Specifically, short time phase fluctuations were seen in radio occultation data by Pioneer Venus mission, and were presumably caused by gravity waves (Woo et al., 1980). More recently, VIRTIS on board VEx observed visible trains of oscillating cloud brightness in the UV for the upper cloud layer (~70 km) on the dayside and around 50 km altitude from the thermal radiation on the nightside (Peralta et al., 2008). These authors detected wavelengths of 60–150 km propagating westward with phase velocities similar to the zonal flow, with no correlation between the location of the waves and surface topography, latitude, local time or structure of the wind. On the contrary, a strong latitudinal dependence of the gravity wave activity was observed by VeRa Radio science experiment on board VEx, with an increasing activity with latitude, probably associated with topography (Tellmann et al., 2012). Also, those results show evidence of local time dependence in the equatorial region (stronger GW activity during daytime), supporting the hypothesis of cloud-level convection as a source of GW in this latitudinal range. Horizontal wavelengths observed by VeRa at 65 km are on the order of 300–450 km, with horizontal phase speeds of roughly 5–10 m/s. In addition, Garcia et al. (2009) detected perturbations in the CO₂ non-LTE emissions expected in the altitude range of 110–140 km by the instrument VIRTIS/VEx. This study reported wave-like structure with horizontal wavelengths of 90–400 km, claimed to be generated from the polar vortex. High latitude (60°–80°) waves of different type (long, medium, short and irregular) have also been

Table 2

Wave characteristics used in the reference simulation. Values in the bracket indicate the extreme of the probability distribution.

Phase Velocity [m/s]	Horizontal wavel. amplitude [km]	EP-flux kg m ⁻¹ s ⁻²	Saturation	Diffusion kg m ⁻¹ s ⁻¹
[1–61]	[50–500]	[0–0.005]	0.85	0.1

identified by the VMC camera on board VEx and assumed to be gravity waves (Piccialli et al., 2014).

Several general circulation models (Bougher et al., 1988; Hoshino et al., 2013; Zalucha et al., 2013; Zhang et al., 1996) also have investigated the effect of gravity waves on the variation of wind velocity in the Venusian lower thermosphere. Bougher et al. (1988) assumed Rayleigh friction and suggested that wave drag would decelerate the SS-AS winds in the thermosphere. In Zalucha et al. (2013), the authors suggested that gravity waves did not propagate above an altitude of about 115 km at the terminator, because of total internal reflection. In the work by Hoshino et al. (2013) the source of gravity waves causing perturbations in the thermosphere is supposed to be at 80 km (near the lower boundary layer of their GCM). They concluded that the westward momentum which drives the retrograde superrotation zonal (RSZ) winds in the nightside around 110 km is provided by gravity waves breaking between 115–130 km altitude.

Encouraged by observational evidence of GW and their potential impact on the upper mesosphere/lower thermosphere of Venus, we implemented a preliminary parameterisation of non stationary (i.e non-orographic) gravity waves for the first time in the LMD-VGCM. At this stage of the work, the main purpose is to reduce the strong jets obtained before the morning terminator at equatorial and low-latitudes and perform more stable runs. In practice, the model is unstable and it stops running when numerical instabilities at some points of the grid produce unrealistic temperatures/densities.

Non-orographic gravity waves on Venus are thought to be emitted above the thick convective layer of the middle cloud region (50–60 km), propagate upwards and break in the thermosphere providing a significant source of momentum and energy (Alexander et al., 1992). In this work we followed the formalism developed for the Earth GCM and described in Lott and Guez (2013) based on a stochastic approach, where a large ensemble of monochromatic GW is generated at a fixed launching altitude by emitting a few waves at each time step, and by adding the effect of these waves to that of the waves launched before. The source of the gravity waves is here chosen uniform, without latitudinal variation, and fixed at roughly 55 km, near the top of the convective layer. The routine is now fully implemented in the code and a detailed sensitivity study to tuneable values used in this GW parameterization will be done in a future dedicated paper. Here we provide the baseline parameters used in the current version of VGCM. Following Lott and Guez (2013) the wave characteristics are chosen randomly, with an arbitrarily fixed probability distribution. As listed in Table 2, the absolute phase speed is between 1 and 60 m/s, the horizontal wave number is between 50 and 500 km (within observational range). The maximum value of the EP-flux at the launching altitude is fixed at 0.005 kg m⁻¹ s⁻². The parameters controlling the breaking (saturation parameter) and the decay of EP-flux (diffusion parameter) are 0.85 and 0.1 kg m⁻¹ s⁻¹, respectively (see Equations (11) and (12) in Lott and Guez, 2013 for details).

3. Results: reference simulations

In this section we describe the results obtained after 10 Venus days (about 3 terrestrial years). All the physical processes and

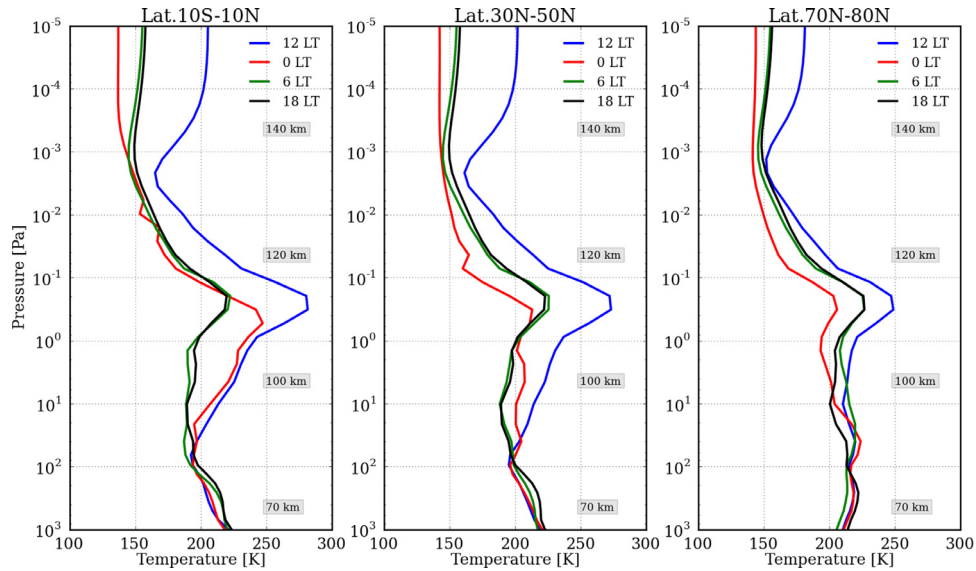


Fig. 3. Reference averaged temperature profiles predicted by the LMD-VGCM at 10^3 – 10^{-5} Pa (about 65–150 km approximately), at equatorial regions (10°S – 10°N) (left panel), mid-latitudes (30°N – 50°N) (middle panel) and at high latitudes (70°N – 80°N) (right panel) at four different local time conditions: midday (blue), midnight (red), morning terminator (green) and evening terminator (black). Approximate altitudes are also indicated in the three panels, as reference. (For interpretation of the references to colour in this figure legend, the reader is referred to the web version of this article.)

the non-orographic GW parameterisation described in the previous sections are included. The initial state is taken from previous simulations on the 0–100 km domain, performed for nearly 1000 Venus days. Above 100 km, the initial horizontal wind is fixed to zero and the initial temperature is set to the 100 km values and held constant until the top of the model.

For the reference simulation we used: 3×10^{-12} $\text{cm}^3 \text{ s}^{-1}$ for the CO_2 -O deactivation rate (k_{v-t}), 23 % for the EUV efficiency, close to the upper limit of standard efficiencies calculated by Fox (1988), and solar cycle “mean” flux values (to compare our results with Venus Express data taken between 2006 and 2014). Sensitivity tests showing the impact of the variation of those key parameters on the thermal structure are shown in Section 5. We describe here the thermal structure predicted by the LMD-VGCM above 100 km, in terms of vertical, diurnal and horizontal variation.

3.1. Thermal balance

The thermal structure predicted by the LMD-VGCM reflects the combined effects of radiative, chemical and dynamical processes. Figs. 1 and Fig. 2 show the components of the thermal balance averaged in equatorial (10°S – 10°N) and mid-latitude (30°N – 50°N) regions, respectively, at four different local times: midday, midnight, morning terminator (MT) and evening terminator (ET). As discussed previously, during daytime, and above 10 Pa (approximately 95 km) the heating occurs via solar absorption by CO_2 near-infrared bands (2.7 μm , 4.7 μm and 1–2 μm), and above 10^{-3} Pa (130 km approximately) EUV absorption dominates. Thermal cooling takes place via CO_2 non-LTE transitions around 15 μm which, together with thermal conduction, competes with the heating terms to control the temperature in the lower thermosphere. The net radiative rate is balanced by the heating/cooling terms obtained from the dynamical core (adiabatic fluid advection, including both horizontal and vertical transport).

At midday and at equatorial regions (Fig. 1), the mean heating rates peak around 0.027 K/s (about 2300 K/Earth day) and 0.058 K/s (about 5000 K/Earth day), for the NIR and EUV rates, respectively. Smaller values are found at high-latitudes (not shown here), related to the decrease of solar radiation with increasing latitudes. The net radiative heating at midday indicates a warm

layer between 1 and 0.1 Pa (about 105 and 110 km) at all latitudes. Radiative balance largely maintains the midday structure, while the dynamical terms are minimal compared to these radiative terms. This behaviour is also simulated by the VTGCM (e.g. Brecht and Bougher, 2012). At other times of the day the net radiative heating is negative. At the terminators the thermal balance suggests a colder thermosphere above 10^{-3} Pa (approximately 130 km), since the solar flux is weaker and hence the EUV heating is not strong enough to balance the thermal conduction. In contrast to daytime, the dynamical heating at the terminator dominates above the other radiative terms. At nighttime, the dynamical rate is slightly stronger at the equator than at higher latitudes, as shown in Figs. 1 and 2. This suggests a link with the vertical downwelling of subsolar-to-antisolar (SS-AS) circulation air at the anti-solar (AS) point. The subsidence, together with the transport from the warm dayside (advection), heats the atmosphere around 0.5 Pa (about 105 km). In addition, radiative cooling is weak at nighttime at those layers.

Those NIR heating/cooling rates are compatible with the results by the VTGCM of Brecht et al. (2011) (see their figure 5) and Brecht and Bougher (2012) for similar latitude-local time conditions. However, the EUV heating rates predicted at daytime by our model are larger by about a factor 2. This is due to the different solar cycle conditions used in the models. These authors used solar minimum fluxes ($F_{10.7}=70$) to compare their simulations with early VEx data, while our simulations assume mean solar conditions. It should also be noted that both models follow RO2000 for the 4.3 μm heating and 15 μm cooling rates, although the parameterisation of these non-LTE processes is different in the models. Moreover, the VTGCM described in Brecht et al. (2011) does not include the coupling between deep and upper regions of the atmosphere, as it is the case in our model. This may play an important role on the whole thermal structure and could partially explain the differences between both models found at the altitudes considered in this paper. In spite of these differences, the cooling and solar heating terms are similar. Nevertheless, a proper model inter-comparison has to be carried out to better explain those discrepancies/similarities between GCMs, as it was done for the Martian GCMs in (González-Galindo et al., 2009).

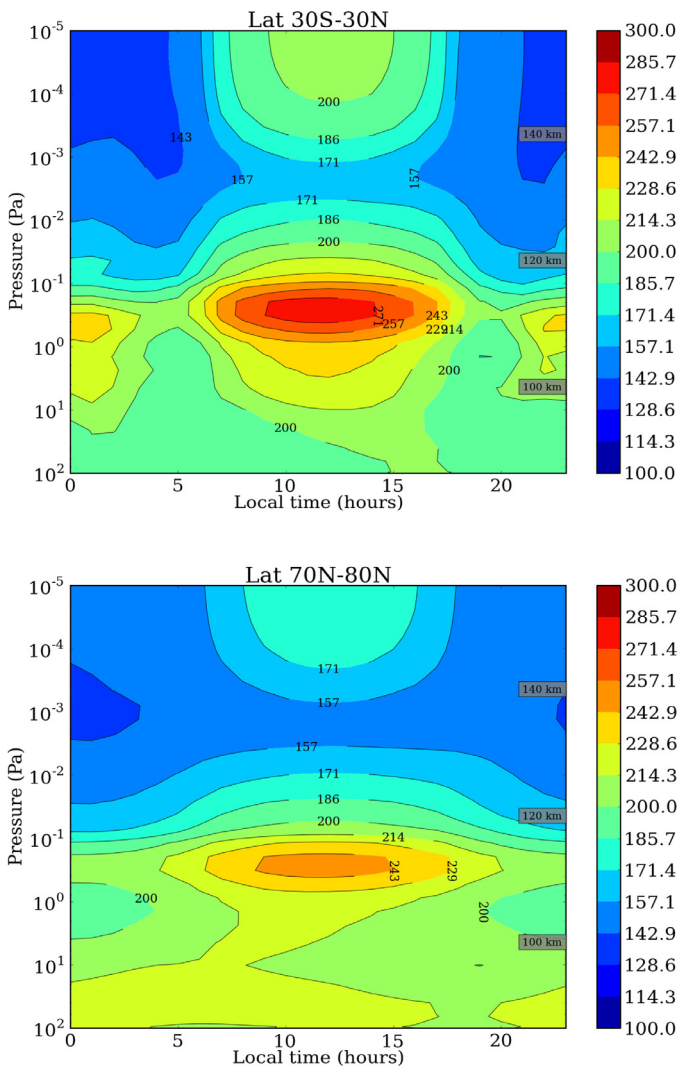


Fig. 4. Local time-pressure cross sections of temperature fields [K] of the reference VGCM simulation after 10 Venus days, averaged at equatorial region 30°S–30°N (upper panel), and high northern latitudes 70°N–80°N (lower panel). Approximate altitudes are also indicated in the two panels, as reference.

3.2. Vertical structure and diurnal variation

The temperature structure of the upper mesosphere/lower thermosphere of Venus is strongly affected by the net day-to-night variation of solar flux, and the vertical structure is therefore strictly linked to the diurnal variation. Fig. 3 shows vertical temperature profiles of the reference simulation at four selected local times (0, 6, 12, 18 LT) in the pressure range 10^3 – 10^{-5} Pa (corresponding to 65–150 km, approximately). The three panels of the figure represent the averaged profiles at equatorial regions (10°S–10°N), at middle (30°N–50°N) and at high (70°N–80°N) northern latitudes. Similar results are obtained at southern latitudes (not shown).

A local warm region is found at dayside mesospheric layers between 1 and 10^{-1} Pa (approximately 105 and 110 km) due to the impact of near IR heating rates during daytime. This warm layer corresponds to the net radiative heating peak shown in Figs. 1 and 2. On the nightside, a warm region around 0.5 Pa (approximately 105 km) whose intensity decreases with increasing latitudes, is predicted by the LMD-VGCM. It is interpreted here as a combination of advection from the dayside and subsidence at the AS-point (see Section 3.1).

Above this warm layer a colder region is produced by $15 \mu\text{m}$ non-LTE CO_2 bands. In the thermosphere the temperature increases due to EUV solar absorption. Also, a cold nightside thermospheric temperature of less than 150 K is found, consistent with the nightside “cryosphere” above 140–150 km observed by Pioneer Venus (Keating et al., 1980; Schubert et al., 1980).

In general, the predicted vertical profile of temperature is in agreement with recent observations by VEx (Gilli et al., 2015; Mahieux et al., 2015; Piccialli et al., 2015) as shown with more details in Section 4, and with other modelling efforts in the upper atmosphere of Venus (Bougher et al., 2015; Brecht and Bougher, 2012; Brecht et al., 2011).

A further insight into the vertical and diurnal variations of the reference LMD-VGCM simulation is gained by analysing the local time maps of latitudinally averaged temperatures versus pressure levels, shown in Fig. 4. The two panels correspond to the average temperatures between 30°S and 30°N and at high northern latitudes, between 70°N and 80°N. The nightside warmer layer between 1 Pa and 10^{-1} Pa (approximately 105–110 km) at equatorial regions is about 30–40 K warmer than at higher latitudes, as expected by strong subsidence at the AS point. This is also clearly visible in the upper panel of Fig. 5a, in which temperature values at 1 Pa are plotted versus local time, for 6 selected latitudes in the northern hemisphere (0°, 16°, 33°, 50°, 67° and 84°). At those levels (~105–110 km), nighttime temperature values at the equator reach about 240 K, which are consistent with the permanent warm mesospheric layer observed by SPICAV/VEx at lower altitudes (90–110 km) (Piccialli et al., 2015). A more detailed discussion is provided in Section 4.

The lower panel of Fig. 5a shows the variation of the ratio $[\text{O}/\text{CO}_2]$ with local time to investigate possible impact on the thermal structure. Two minima of temperature (about 190 K and 195 K) predicted at 4–5 LT and at 19–20 LT, just before the morning terminator and after the evening terminator, respectively, are not linked to this ratio but to upward transport and strong zonal winds, as it will be detailed in Section 3.5. Fig. 5a also shows a strong enhancement of atomic oxygen at night, peaking at midnight. This is produced by the efficient day-to-night transport and it corresponds to the subsiding region (i.e. local warm region). Similarly, Fig. 5b shows the diurnal evolution of the temperature and the ratio $[\text{O}/\text{CO}_2]$ near the top of the model (approximately 140 km). The LMD-VGCM predicts a nightside equator-to-pole warming (up to 15 K) at those altitudes. Figs. 1 and 2 suggest that this trend is due to dynamical heating in the lower thermosphere (in the absence of other heating processes at nighttime). This emphasises the large role of dynamical processes in the evolution of the thermal structure and composition in the upper atmosphere of Venus, notably throughout nighttime and terminators, while during daytime radiative processes dominate at all altitudes. This importance of dynamical and radiative processes is also simulated by the VTGCM (Brecht and Bougher, 2012).

3.3. Latitudinal variation

Fig. 6 shows the mean temperature fields as function of pressure and latitude, for different local time conditions. Temperature is averaged for each Local Time and pressure level (i.e. in a Solar-fixed reference frame) and the associated standard deviation (not shown here) is in general less than 1K, except in the upper mesosphere (~100–120 km) before dawn, where it is up to 2K. A further insight into the latitudinal variation is given in Fig. 7, showing the local time-latitude cross sections at six reference pressure levels (10^{-4} Pa, 10^{-3} Pa, 10^{-1} Pa, 1 Pa, 5 Pa, 10 Pa), covering the upper layers of the atmosphere of Venus studied in this work (from 95 to 140 km altitudes, approximately).

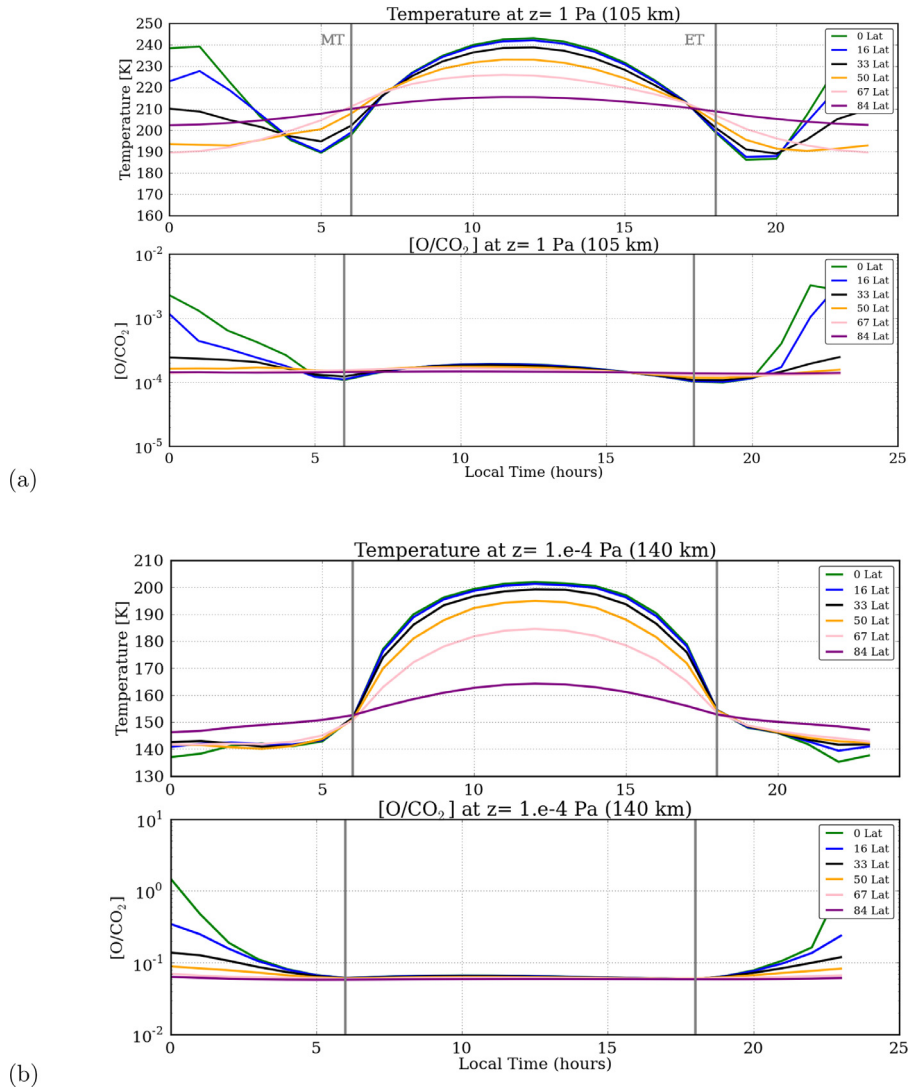


Fig. 5. Panels (a) Diurnal variation of reference temperature (upper panel) and ratio $[O/CO_2]$ (lower panel) at a constant pressure (1 Pa) corresponding to 105 km approximately, at six selected latitudes in the northern hemisphere: equator (green), 16°(blue), 33°(black), 50°(yellow), 67°(pink), 84°(purple). Panels (b) Same as in (a) but at the constant pressure level 10^{-4} Pa (140 km approximately). (For interpretation of the references to colour in this figure legend, the reader is referred to the web version of this article.)

During daytime (7–17 LT), in general the model predicts a decreasing temperature from the SS point to higher latitudes at all altitudes in the upper mesosphere/lower thermosphere. This trend is in good agreement with VIRTIS/VEX daytime nadir observations described in Peralta et al. (2016) and with other model results by Brecht and Bougher (2012), although the intensity of the maximum around the SS point differs, being up to 40 K larger in our model than in Brecht and Bougher (2012). However, this value is in agreement with the observational range obtained by ground-based telescopes as reported in Sonnabend et al. (2010) and Krause et al. (2016). Our predicted local maximum between 1–0.1 Pa at daytime peaks around 280 K at the SS point and it decreases by about 50 K near the poles.

At terminators (left panels of Fig. 6) the latitudinal variation of the temperature above 10^{-1} Pa (110 km approximately) is rather small, in overall agreement with SOIR/VEX observations and with the VTGCM results (Bougher et al., 2015; Mahieux et al., 2015). Maps in Fig. 7 show that in the mesosphere, around 10 Pa (panel f), a colder region is found at mid-low latitudes (40°S–40°N) near the terminator. This structure evolves and propagate upwards ac-

ordingly to the strength of the zonal winds at those altitudes, as discussed in Section 3.4.

At nighttime, the warming predicted at mesospheric altitudes (see previous sections) is stronger at the equator than at higher latitudes, confirming a strong subsidence at the anti-solar point. Above 10^{-1} Pa the latitudinal trend is inverse: the atmosphere is up to 15 K warmer at polar regions than at equator latitudes (see also panels a, b and c in Fig. 7). Unfortunately, this variation cannot be validated yet with available measurements: nighttime observations by SPICAV/VEX are scarcer at polar regions compared to equatorial measurements.

3.4. Impact of gravity waves parameterisation on the thermal structure: a preliminary study

Fig. 8 shows the impact of our parameterisation of non-orographic gravity waves (see Section 2.8) on the thermal structure and winds predicted by the LMD-VGCM around 105 km (1 Pa). Simulations performed without non-orographic GW are compared with those obtained including this parameterisation (after 3Vd and 10Vd). The tuneable GW parameters used here are listed in Table 2.

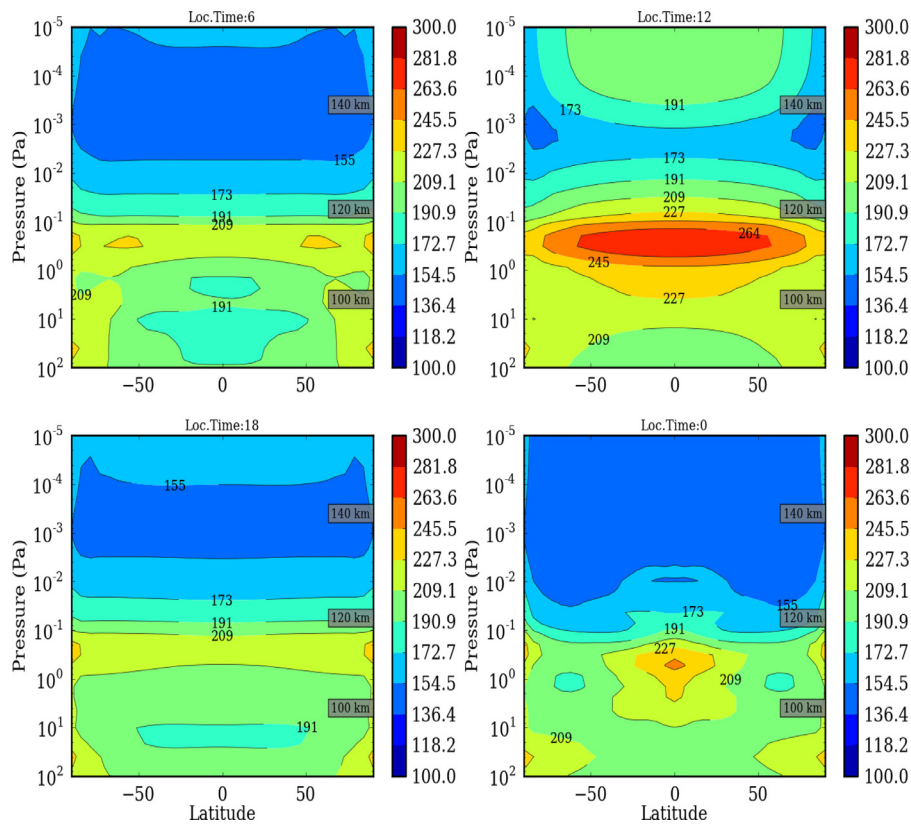


Fig. 6. Latitude-pressure cross sections of reference simulated temperatures [K] at morning terminator (6 LT), midday (12 LT), evening terminator (18 LT) and midnight (0 LT), as indicated. The pressure levels (10^2 – 10^{-5} Pa) correspond to 80–150 km altitude, approximately.

The cold region visible between 2–5 LT in the temperature field in the left column (no GW) is produced by strong equatorial jets and vertical ascending flux from the lower to the upper mesosphere. These jets are noticeably reduced after the non-orographic GW scheme implementation (second and third column), notably comparing simulations after the same day (3 Vd). Both zonal and vertical winds are smoothed at mid-high latitudes by the GW propagation, and consequently the formation of the cold upwelling pool is delayed and weakened (see results after 10 Vd). Its origin and evolution remains to be explored in a dedicated paper but it is either linked to angular momentum transport by the thermal tides, or to planetary scale waves propagation from the lower mesosphere. The current GW parameterisation, even if preliminary, helps reducing the temperature differences between MT and ET, which are not observed in the data.

A number of sensitivity tests have been performed to evaluate the impact of GW tuneable parameters on the thermal structure, in particular those linked to the waves characteristics, still not well constrained by observations. For example, we found that GW are mostly absorbed where zonal winds are stronger (i.e. near the terminator). Gravity waves slightly accelerate the zonal wind field in the region of its peak (around 10^3 Pa) and decelerate it at higher layers. The higher the relative phase velocity, the larger this effect. Moreover, larger horizontal amplitude GW deposit less momentum than smaller waves. GW with larger initial vertical momentum flux are rapidly absorbed near the launching altitude and they inject more kinetic momentum compared to waves of the same characteristics (phase velocity amplitude, horizontal wavenumber, launching altitude). As a consequence, they decelerate the zonal winds in the whole atmosphere.

In conclusion, the variation of the main parameters used in the GW routine (i.e., wave characteristics, saturation, wave dissipation

parameters, vertical momentum flux) has a significant impact on the stability of the model, since it reduces (or amplifies) the evolution of the dynamical structure discussed in previous section and its effect on the atmospheric layers above 90 km. The criteria to select the waves characteristics values in this work was consistency with the limited observational constrains (altitude of the source, waves amplitude, phase velocity) and a better agreement with observed temperature values at the terminator.

3.5. The transition region: key to understand the variability of the upper atmosphere

Recent VEx observations revealed a surprisingly more variable upper atmosphere (Gérard et al., 2014; Soret et al., 2014) notably between 90 and 120 km, were RSZ flow and day-to-night circulation overlap. Our model simulations can help to investigate the exchanges between the deep atmosphere and the upper layers, and to study the specific processes responsible for driving the variations in this puzzling “transition” region. The latitude-local time maps at a constant pressure ($z = 1$ Pa) in Fig. 8 exhibit the strong correlation between temperature, zonal winds and vertical transport in that region. This is particularly discernible in the left column of the figure, showing results without the GW implementation. In that case, strong RSZ winds (up to 250 m/s) shift the cold air westward and consequently the vertical upward flux does not match perfectly the cold temperature region.

We suggest a link between the angular momentum transport by the thermal tides and the upwelling before the morning terminator. A detailed wave analysis by the LMD-VGCM presented in Lebonnois et al. (2016) confirmed the role of diurnal and semi-diurnal tides in vertical angular momentum transport in the upper clouds, as shown before in L10. Above 10^2 Pa (about 80 km) at high latitudes diurnal tides dominate, while between 10^4 and 10^2

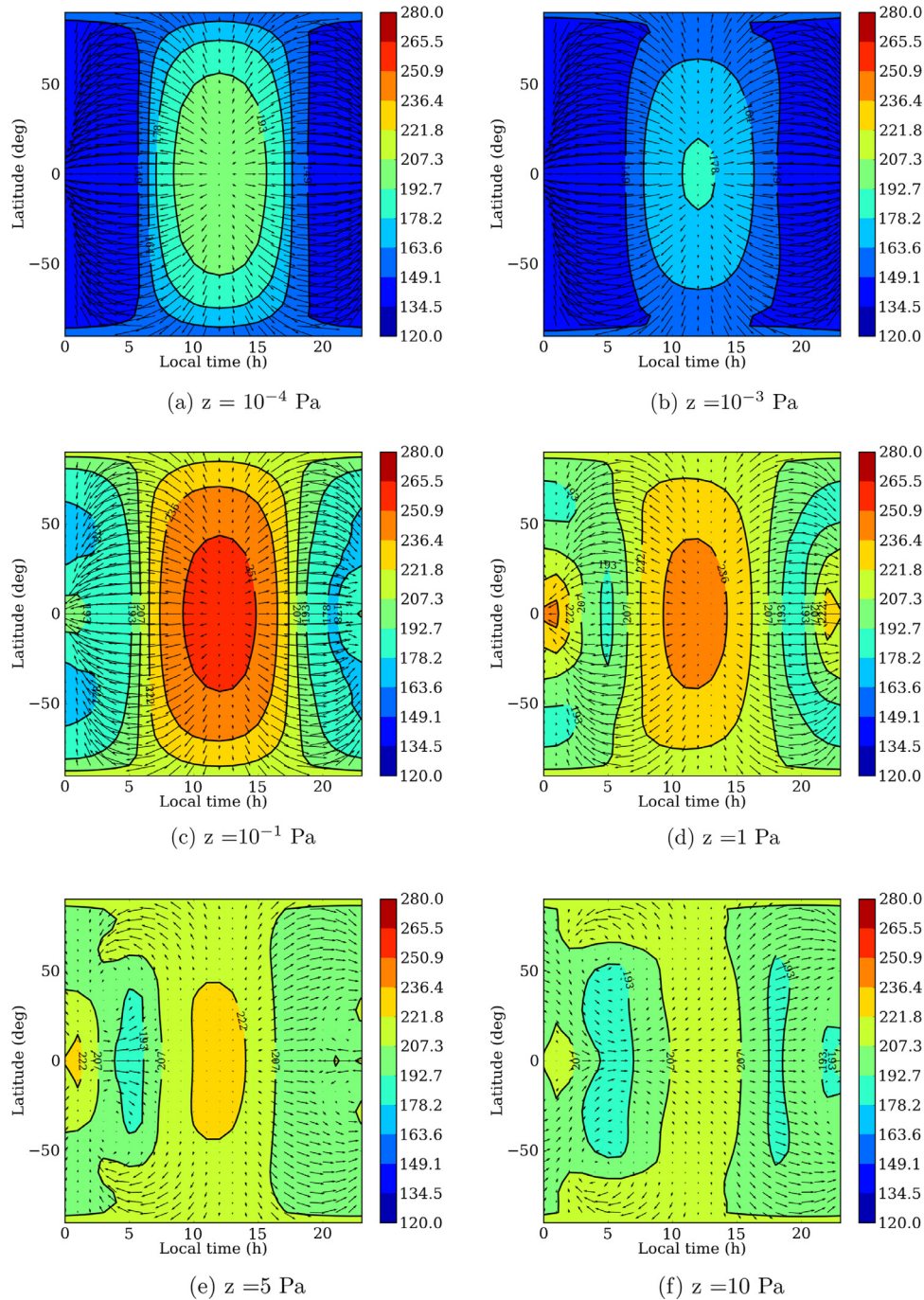


Fig. 7. Local time-latitude cross sections of longitudinally averaged temperature fields [K], after 10 Vd at six different pressure levels: as indicated. They correspond to 140 km (a), 130 km (b), 110 km (c), 105 km (d), 100 km (e) and 95 km (f) altitudes, approximately.

(60–80 km, approximately) at low-middle latitudes a combination of semi-diurnal tides and vertical transport prevails. However, it must be kept in mind that in the simulations described here, the zonal wind below the clouds is a factor 4–5 weaker than observed. This certainly affects the angular momentum budget in the cloud region, but it may also have an impact on the circulation in the layers above, in particular in the transition region discussed here.

4. Comparison with VEx and ground-based temperatures above 100 km

In this section we compare our reference simulation, performed after 10 Venus days, with a selection of Venus Express and ground-

based retrieved temperatures. Data and simulations in Figs. 9–11 are averaged in mid-latitudes bins (30°N and 50°), at different local time conditions. The comparison is performed in altitude instead of pressure coordinates, since the selection measurements used here (i.e. solar/stellar occultation, limb measurements) are taken in function of altitudes.

For the dayside (7–17LT) the measurements are very scarce and uncertain. Fig. 9 shows available daytime retrieved temperatures above 100 km altitude from CO IR non-LTE emissions around 4.7 μm observed by VIRTIS/VEx (Gilli et al., 2015), and ground based observations of heterodyne CO₂ emissions at 10 μm , around 110 km by THIS/HIPWAC (Wischniewski et al., 2015). As represented

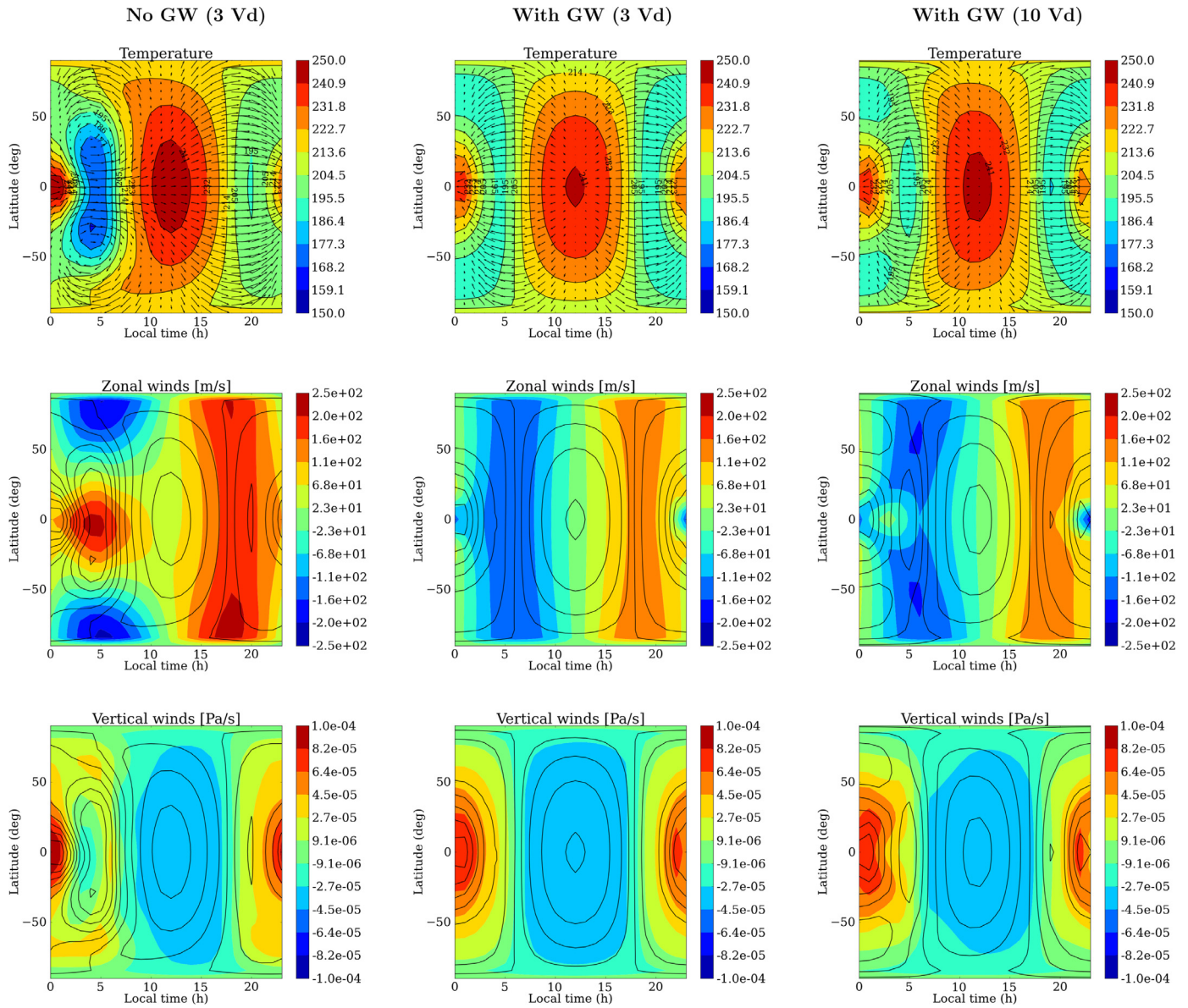


Fig. 8. Latitude-local time cross section of longitudinally averaged temperature [K], zonal wind and vertical fields, without (left column) and with the inclusion of a GW parameterisation (middle and right columns), after 3 Vd and 10 Vd, as indicated. Pressure level is 1 Pa (105 km approximately) in all panels. Positive zonal wind values are westward, and positive vertical wind values correspond to downward motion. Temperature field contours (black lines) are over-plotted in all panels and wind vectors (in m/s) only in the upper panels.

in the figure, VIRTIS errors bars (30–40 K) and the variability observed by ground-based telescopes are very large. Thus, it is difficult to draw strong conclusions, but the model results are within error bars at almost all altitudes. Compared to the VTS3 reference model, both LMD-VGCM and the observed temperatures are warmer below 125 km altitude, and colder above.

At nighttime (19–5LT), SPICAV/VEX averaged profiles in the latitude boxes 30°N–50°N and 30°S–50°S (updated from Piccialli et al., 2015) are shown in Fig. 10, with standard deviation bars. Also, the VTS3 model at nighttime is plotted as reference. LMD-VGCM temperatures are generally larger than observations and VTS3 values everywhere above 100 km. Moreover, the vertical variation of temperature in the VGCM is different from SPICAV data below about 120 km, although the intensity of the peak is similar in the model and in the observations (around 210 K). One explanation is that the apparent warm layer found by SPICAV between 90–100 km is instead predicted by our model at higher altitudes. Another possibility is that our model produces too strong heat-

ing around 110 km. Above 120 km, at thermospheric altitudes, LMD-VGCM nighttime simulations are about 30 K warmer than observed, probably caused by a too strong dynamical heating in the model. Gravity-wave induced drag might produce the deceleration of the day-to-night winds necessary to isolate the dayside and nightside sufficiently to yield the observed cryosphere (Alexander et al., 1992; Bougher et al., 1997). Therefore, it is possible that the GW drag on the SS-AS component is not strong enough in our simulation to reduce the temperature on the nightside. A detailed sensitivity study of the model to GW parameters is foreseen in future works.

Regarding the terminator, SOIR averaged profiles (6 and 18 LT) in the selected latitude boxes from Mahieux et al. (2015) and ground-based observations from THIS/HIPWAC (Krause et al., 2015) around 110 km are shown in Fig. 11, together with model predictions. Similar to daytime conditions, a succession of warm and cold layers is found in both observed and predicted profiles, reflecting the combined influence of radiative features and global circulation.

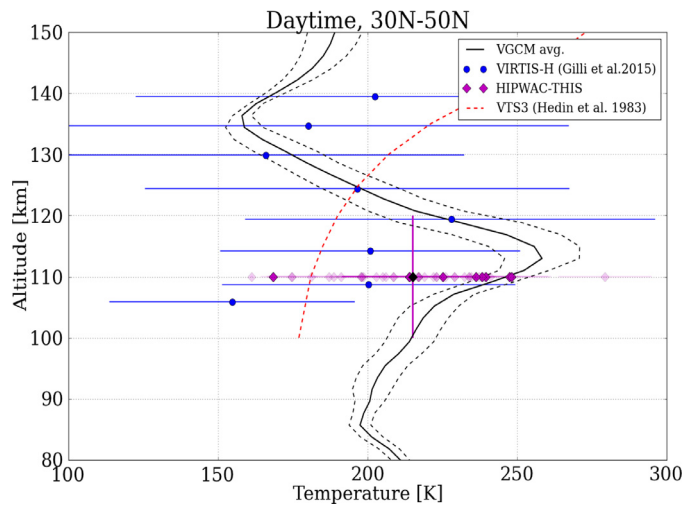


Fig. 9. Temperature vertical averaged profiles as function of altitude, predicted by the LMD-VGCM in the latitudinal range 30°N–50°N (solid black line) at midday (10–12 LT), with standard deviation (dashed black line), together with VIRTIS/VEx temperature retrieval results (blue circles) and error bars at the same latitude and local time boxes. (extracted from Fig. 14 in Gilli et al., 2015). Temperature results at approximately 110 km from ground based observations in Wischniewski et al. (2015) are shown in purple. The model VTS3 by Hedin et al. (1983) at daytime is also plotted (red dashed line), as reference. (For interpretation of the references to colour in this figure legend, the reader is referred to the web version of this article.)

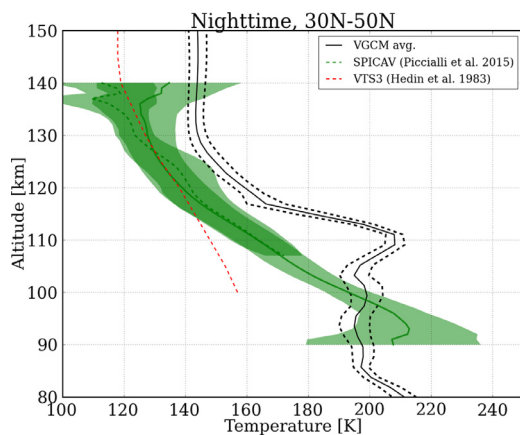


Fig. 10. Temperature vertical averaged profiles as function of altitude, predicted by the LMD-VGCM in the latitudinal range 30°N–50°N (solid black line) at nighttime (19–5 LT), with standard deviation (dashed black line), together with SPICAV/VEx temperature retrieval results (in green): 30°N–50°N (dashed line) and 30°S–50°S (solid line). Standard deviations are also represented with the shaded green area (after Piccialli et al., 2015). The model VTS3 by Hedin et al. (1983) at nighttime is also plotted (red dashed line), as reference. (For interpretation of the references to colour in this figure legend, the reader is referred to the web version of this article.)

In spite of the large variability exhibited by SOIR measurements (20–30 K), significant data-model differences may be discerned. First, our simulations are warmer (up to 30 K) between about 110 and 125 km altitude, while thermospheric temperatures predicted above 135 km are 40–50 K colder than observed. Second, as also noticed at nighttime, our model predicts a mesospheric peak at higher altitudes compared to observations.

Those discrepancies are investigated by means of sensitivity studies in the next section.

5. Sensitivity tests to input parameters

Several sensitivity tests have been performed in order to evaluate the impact on the thermal structure predicted by the LMD-

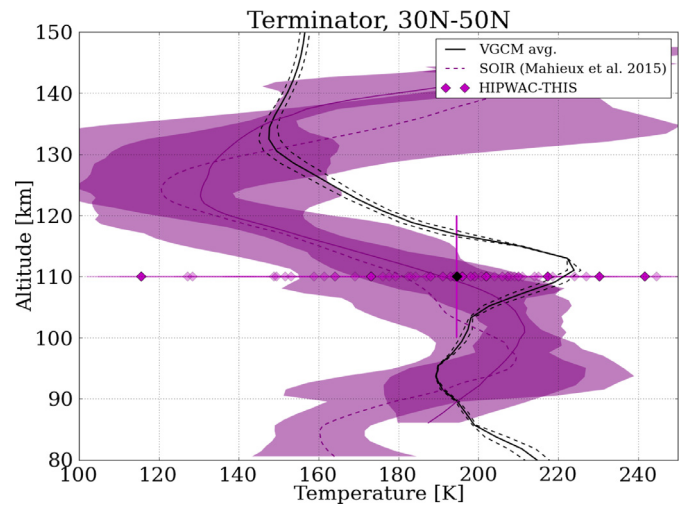


Fig. 11. Temperature vertical mean profiles as function of altitude, predicted by the LMD-VGCM in the latitudinal range 30°N–50°N (solid black line) at the terminator, with standard deviation of the mean (dashed black line), together with SOIR/VEx temperature retrieval results (pink dashed line for the morning and solid for the evening terminator) at the same latitudes bin. SOIR standard deviations are also represented with shaded pink area (after Mahieux et al., 2015). Temperature results at 110 km from ground based observations (Krause et al., 2015) are also shown in purple. (For interpretation of the references to colour in this figure legend, the reader is referred to the web version of this article.)

VGCM of the uncertainty of the main model input. Figs. 12 and 13 show the sensitivity to three of the main radiative input parameters: the EUV solar flux, the CO₂-O deactivation rate, and the near-IR non-LTE heating rate. Results obtained at the equatorial region (10°S–10°N) at midday (12 LT) are shown in Fig. 12, for both thermal balance and temperature, as representative of daytime conditions. Fig. 13 shows the impact of those parameters on the temperature profiles, at midnight (0 LT) and evening terminator (18 LT), at equatorial regions. The variation of the first two parameters (EUV solar flux and quenching rate coefficient) affects only the layers above approximately 125 km (10⁻² Pa) for all local times. In contrast, changes in the SHR parameterisation play a role mainly in the mesosphere during daytime, but also in the thermosphere at nighttime and at terminator through heat transport from the daytime.

5.1. EUV solar flux

Compared to the reference temperature profiles described in Section 3, calculated for mean solar cycle conditions, the solar cycle maximum/minimum conditions produce an increase/decrease of temperatures up to 25 K above 135 km during daytime, and less than 10 K at the terminator. This indicates that the solar activity alone cannot explain the 40–50 K difference between data and our model at the terminator in the thermosphere. In addition, Fig. 13 shows that the variation of the EUV solar flux has no impact on the temperature profile at nighttime. Another parameter whose uncertainty may affect the temperature in the thermosphere is the EUV efficiency (not shown here): a variation of 5% produce changes of temperatures of about 10–12 K during daytime (smaller at other local times).

5.2. Collisional rate coefficient $k_{\nu-t}$

The uncertainty in the knowledge of the deactivation/collisional rate coefficient $k_{\nu-t}$ used in the 15 μ m cooling could partially explain the discrepancies between VEx temperatures and model simulations at thermospheric layers. The uncertainty brackets values from $1 \times 10^{-12} \text{ cm}^3 \text{ s}^{-1}$ to $6 \times 10^{-12} \text{ cm}^3 \text{ s}^{-1}$. As shown in the fig-

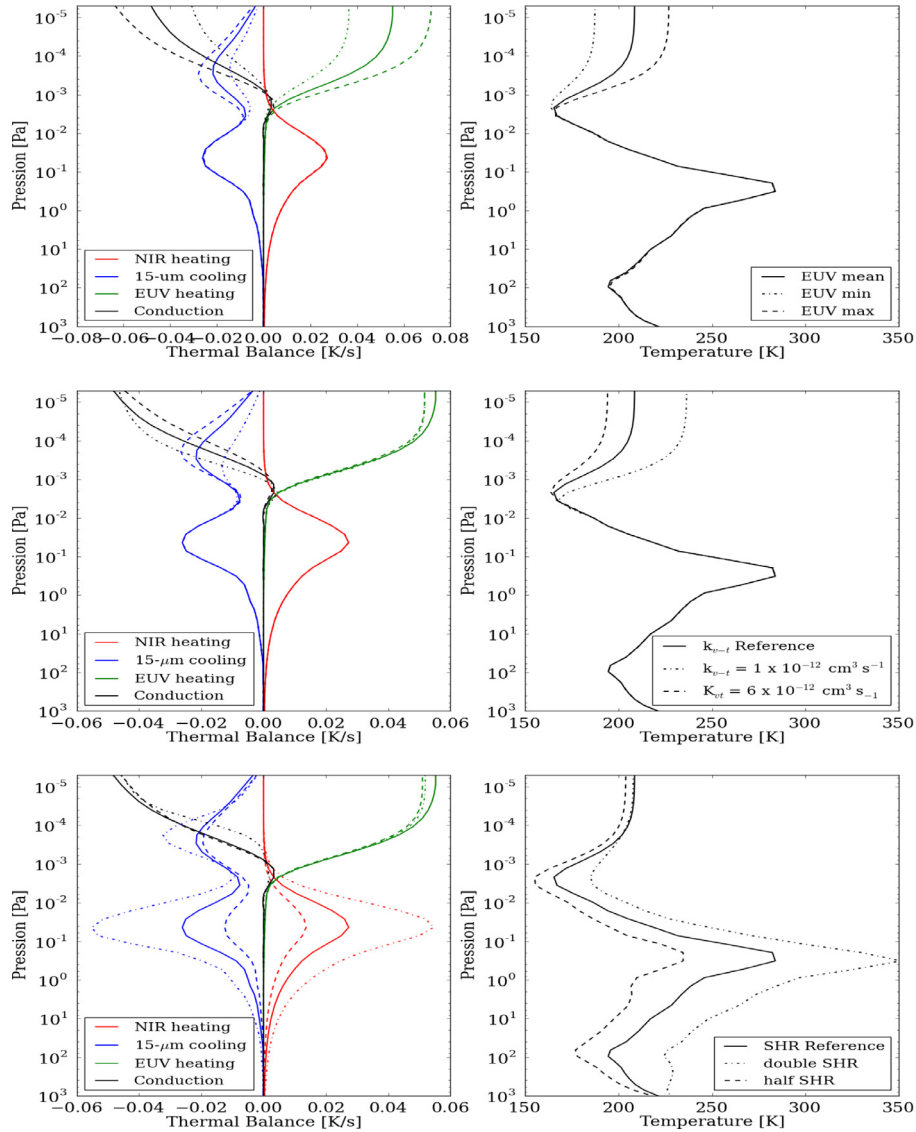


Fig. 12. Sensitivity tests to some model input parameters. Thermal balance (left panels) and vertical temperature profiles (right panels) at midday (12 LT), averaged in the latitude box 10°S – 10°N are shown as function of pressure (corresponding to 65–150 km altitudes, approximately). The reference simulation is plotted in solid lines. Upper panels: variation EUV solar cycle conditions (“minimum” dotted-dashed line, “maximum” dashed line). Middle panels: variation of the quenching rate coefficient k_{v-t} (“maximum” dashed line, “minimum” dotted-dashed line). Lower panels: variation of the Solar Heating rate (“doubled” dotted-dashed line, “halved” dashed line).

ures, the smaller the rate coefficient k_{v-t} , the weaker the cooling above 125–130 km. The increase in temperature with respect to the reference simulation values is up to 30 K at all local times. This test indicates that a lower value of k_{v-t} would reduce the data-model discrepancy and improve the comparison above 130 km at daytime and at terminator. However, at night the radiative cooling at 15 μm competes with the dynamical and the conduction terms, and a smaller k_{v-t} would also produce larger temperature, therefore amplifying the data-model difference.

5.3. Non-LTE solar heating

The last sensitivity tests shown in the Figs. 12–13 (bottom panels) concerns the efficiency of the non-LTE solar heating by CO_2 bands in the near-IR. The solar heating rate (SHR) has been multiplied/divided by a factor 2 and the effect on the thermal structure is to enhance/reduce the intensity of the local temperature maximum mainly at mesospheric altitudes. The changes of the temperature profiles around the mesospheric peak are up to 70 K at daytime, and up to 40 K and 30 K, at the terminator and nighttime,

respectively. The increase/decrease in SHR only affects the magnitude of the peak of temperature, not the altitude. In other words, a reduction of SHR with respect to our “reference” rates (based on Roldán et al., 2000) would produce a better agreement with data for all local times below about 125 km. However, the altitude of temperature peak at mesospheric layers does not change since it is strictly linked to the altitude of the NIR heating peak (i.e related to the choice of the parameters described in Section 2.2). Further modelling efforts are required to improve this non-LTE parameterisation by a fine-tuning process which fulfils both a good match with the LTE conditions and the stability of the model.

These tests also show that radiative processes play only a partial role in the thermal balance of the Venus upper atmosphere, and that the contribution of dynamics should be better investigated to improve the comparison with the observations. On-going work on the impact of the GW parameterisation on winds and temperatures is very promising and a dedicated study is foreseen to evaluate the impact of tuneable GW parameters on the winds and to reach a better agreement with observations.

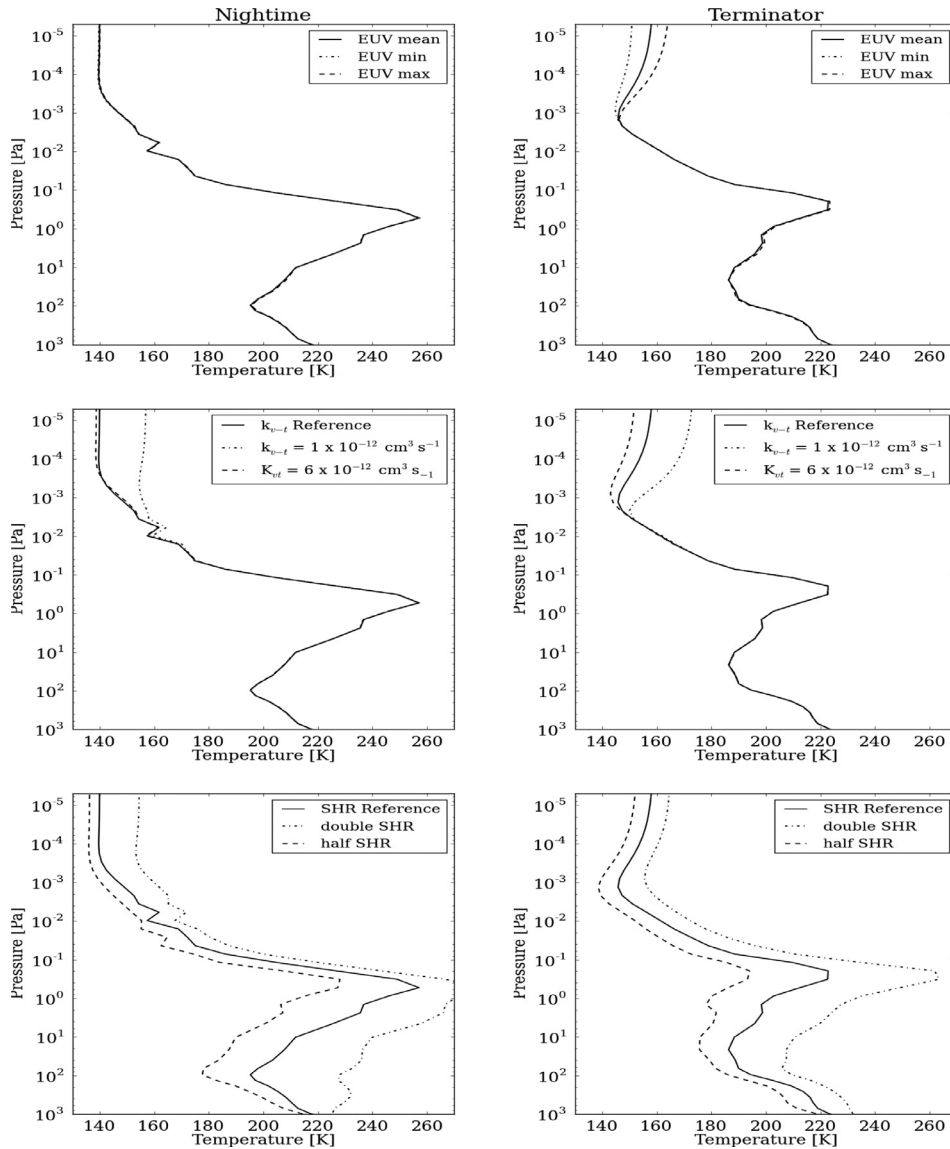


Fig. 13. Same as in Fig. 12 but at nighttime (left column) and at evening terminator (right column).

6. CO and O density results

Although this work is mainly focused on the VGCM predicted thermal structure, other valuable insights can be obtained from the model. Noticeably, a better understanding of modelled atmospheric variables, as winds and composition, helps to constrain temperature fields. As also shown by González-Galindo et al. (2013) in the case of Mars GCM, temperatures in the upper mesosphere/thermosphere are more consistent with observations when temporally and spatially variable atomic oxygen concentrations are used.

Our aim here is to check the composition of the upper atmosphere calculated by the LMD-VGCM. In particular, the atomic oxygen thermosphere content is an important parameter of the 15 μm routines. For this purpose we have compared our CO and O abundances with available VEx observations. These two species are both produced in the Venus upper layers during daytime by CO₂ photodissociation and are thought to be rapidly transferred to the nightside by subsolar-to-anti-solar circulation (Bougher et al., 2006; Clancy and Muhleman, 1985; Lellouch et al., 1997). They both serve as sensitive tracers of transport in the lower thermosphere, in particular they can be used to monitor the large

scale circulation patterns between 90–120 km (the atomic oxygen through O₂ infrared airglows analysis) (Soret et al., 2012). Simulated density profiles shown in Fig. 14 represent averages in the equatorial region (10°S–10°N) at three LT conditions (0, 12, 18 LT).

A selection of CO measurements obtained at similar latitude-local time bins are also plotted. Daytime CO densities are extracted from the work of Gilli et al. (2015) where VIRTIS/VEx non-LTE CO emissions around 4.7 μm were used, while at the terminator an average profile at equatorial regions (0°–30°N) from SPICAV/VEx retrievals (Vandaele et al., 2016) is considered. Typical measurement error bars (not shown) are a factor 10 lower than the densities, but they increase above 130 km. Indirect atomic oxygen density measurements can be deduced from O₂ night-glow emissions observed by VIRTIS/VEx. The O profile in Fig. 14 (bottom panel) is extracted from Fig. 7 in Soret et al. (2012), and it represents -24°S latitude. Measured O density profile averaged at latitudes 10°S–10°N are not yet available in the literature.

Atomic oxygen concentrations predicted by the LMD-VGCM peak at nighttime around 100 km. This is consistent with the profile by Soret et al. (2012), with VTGCM results by Brecht et al. (2012) (see their Table 2) and with the photochemical model by Krasnopolsky (2012). The agreement with the measured

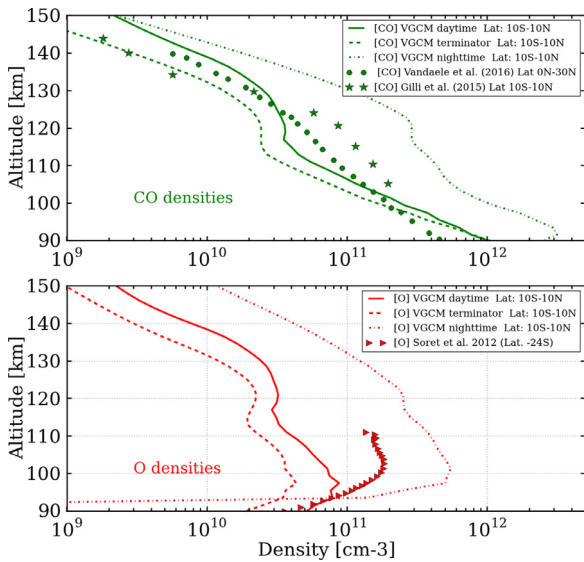


Fig. 14. Density profiles of CO (top panel) and O (bottom panel) predicted by the LMD-VGCM, averaged in equatorial regions (10°S – 10°N) for different local time conditions: LT=12 (solid lines), LT= 18 (dashed lines) and LT= 0 (dotted-dashed line). CO abundances retrieved from Venus Express observations are shown for comparison: VIRTIS/VEx measurements at midday, in the latitude range 10°S – 10°N (Gilli et al., 2015) and SOIR/VEx densities at the terminator, averaged in the latitude range 0 – 30° (Vandaele et al., 2016). O density profile (00:44 LT, -24°S) from Soret et al. (2012) is also showed with triangles.

range 1 – $5 \times 10^{11} \text{ cm}^{-3}$ by VIRTIS/VEx (C erard et al., 2009) is generally good except at the anti-solar point, where our densities are larger than observed (about a factor 2).

Focusing on CO data set below 130 km (with smaller error bars), daytime values are up to a factor 2 larger than at terminator, with a discernible change of slope of the vertical gradient between 110 and 120 km, as also observed at similar layers (Vandaele et al., 2016). Again, a good agreement is found with results by a photochemical model (Krasnopolsky, 2012). Nighttime CO abundances are up to a factor 7 larger than daytime above 100 km, and a nighttime mesospheric bulge is predicted by our model around 95 km, in agreement with observations by ground based telescopes (Clancy et al., 2012; Gurwell et al., 1995). In the altitude region between 100 and 120 km model profiles are smaller than observed values, both at daytime and terminator.

This is partially an effect of thermal structure: smaller temperatures ($\sim 40 \text{ K}$) than predicted lead to larger densities (about 25%) at those altitudes. Another possible reason to explain those discrepancies is that the SS-AS component of the wind is too strong in the model at about 100–120 km, and CO is too rapidly transported from the dayside to nightside. This interpretation also explains the larger LMD-VGCM nighttime temperatures at the same altitudes. A too strong SS-AS circulation in the model also leads to an overestimation of nighttime atomic oxygen. Larger abundances of O above 100 km would cool the temperature by CO_2 collisional quenching above about 130 km. But as demonstrated in Section 5, the increasing of the CO_2 -O deactivation rate (i.e increasing the O abundances by the same factor) should be much larger than a factor 2 to have a considerable impact on the temperature in the thermosphere at nighttime.

7. Summary and conclusions

Current GCMs simulations indicate that both radiative and dynamical effects play a crucial role in determining the thermal structure of the upper atmosphere of Venus, and that previous 1D models (e.g VTS3) are unable to describe the high variability observed by VEx instruments at those altitudes. The GCM used here

is an improved and extended version of the model described in Lebonnois et al. (2012); 2010) and it is the only existing ground-to-thermosphere Venus GCM. It includes the main processes contributing to the thermal balance of the atmosphere of Venus from 90 to 150 km (i.e IR heating by CO_2 , IR CO_2 15 μm cooling, extreme UV heating, thermal conduction, molecular diffusion) as well as a photochemical model (Stolzenbach et al., 2014) and a gravity wave parameterisation Lott and Guez (2013).

The main radiative and dynamical features predicted by our model are consistent with current literature. Focusing on the thermal structure, a succession of warm and cold layers is found, in agreement with VEx observed trends and simulations performed with the VTGCM by Bougher et al. (2015); Brecht and Bougher (2012); Brecht et al. (2011). High temperatures produced by EUV absorption above 140–150 km sit on top a cold layer around 125–130 km, where the 15 μm cooling also plays a role in the thermal balance. Below that region, a local maximum produced by solar absorption by CO_2 IR bands during daytime is then advected to the terminator and to the nighttime. The net radiative heating and the dynamical heating indicate a persistent warm layer between 100 and 120 km at all local times and latitudes.

Decreasing temperatures with increasing latitudes are predicted during daytime at all altitudes above 100 km. Above 110 km (10^{-1} Pa) this latitudinal trend is inverse at nighttime, with an atmosphere up to 15 K warmer towards the pole. However, this variation is smaller than the errors in the available measurements and it cannot be confirmed by data comparison. At the terminator the variation is small, as also observed by SOIR/VEx. Below 110 km, the nightside warm layer predicted by our GCM around 105 km (about 0.5 Pa) is interpreted as a combination of advection from the dayside and subsidence at the AS-point, similar to that described by the VTGCM (Brecht and Bougher, 2012). The cold thermosphere (less than 150 K) detected at night by Alexander et al. (1992) is reproduced by our model. Daytime temperatures are in reasonable agreement with the measurements in the thermosphere, taking into account the large measured error bars. CO and O density results by the LMD-VGCM have been also compared to a few observations, and an overall good agreement is found both in order of magnitude and shape of profiles.

Significant data-model discrepancies may be also discerned. First, thermospheric temperatures (above 135 km) at the terminators are about 40–50 K colder than measured by SOIR/VEx, while nighttime temperatures at similar altitudes are up to 30 K warmer than observed by SPICAV/VEx. Second, the temperature maximum in the mesosphere (between 100 and 120 km) is higher than observed by VEx (between 90 and 110 km), although in good agreement with 3D model results by Brecht and Bougher (2012).

CO density profiles predicted by our model are smaller than selected measurements (VIRTIS/VEx and SOIR/VEx) between 100 and 120 km, both at daytime and terminator. Simulated O density at nighttime are larger than observed (about a factor 2) above about 100 km. This may indicate that the SS-AS component of the winds is too strong in the model at those altitudes and the CO (and O) is too rapidly transported from the dayside to nightside. This interpretation might also explain the larger nightside temperatures in the thermosphere.

Sensitivity tests to input radiative parameters show that a reduction of radiative cooling rate at 15 μm (an increase of temperatures) would improve the data-model comparison at daytime and terminator above about 130 km, but not at nighttime. In addition, the solar activity alone is not able to explain the 40–50 K differences at the terminator in the thermosphere, and the variation of the solar heating rate only affects the magnitude of the peak, but not the altitude. Further modelling efforts are required to improve the non-LTE parameterisation currently implemented in the LMD-VGCM. In addition, these tests indicate that dynamical effects have

to be further studied to improve the comparison with the observations and that radiative processes have a major role in the thermal balance of the Venus upper atmosphere only during daytime.

A first effort to improve data-model comparison was done here by implementing into the Venus GCM a non-orographic GW parameterisation. The comparison with measured temperatures is noticeably improved at terminators. However, the GW drag on the SS-AS component is still weak. A full sensitivity study to GW parameters with the VGCM is the next step. This work is very promising since it will help understanding the large observed variability in the upper atmosphere and its interaction with the layers below. In addition, future work is ongoing at LMD to develop a mesoscale model for the VGCM, based on the same physics as the GCM. This will also allow a better constraint of the GW parameterisation and to take into account the variation of the distribution, amplitude and intensity of the gravity waves, which are currently largely uncertain.

Acknowledgements

G. Gilli has been supported by CNES postdoc grant. F. González-Galindo and M.A. López-Valverde thank the Spanish MINECO for funding support through the CONSOLIDER program “ASTROMOL” CSD2009-00038 and through project AYA2011-23552/ESP. We also thank E. Millour for his technical support with the model, and two anonymous referees for constructive reviews.

References

- Alexander, M.J., Stewart, A.I.F., Bougher, S.W., 1992. Local-time asymmetries in the venus thermosphere. *LPI Contribut.* 789, 1–2.
- Altieri, F., Migliorini, A., Zasova, L., Shakun, A., Piccioni, G., Bellucci, G., 2014. Modeling VIRTIS/VEX O_2 nightglow profiles affected by the propagation of gravity waves in the venus upper mesosphere. *J. Geophys. Res. (Planets)* 119, 2300–2316. doi:10.1002/2013JE004585.
- Bougher, S.W., Alexander, M.J., Mayr, H.G., 1997. Upper atmosphere dynamics: global circulation and gravity waves. In: Bougher, S.W., Hunten, D.M., Phillips, R.J. (Eds.), *Venus II: Geology, Geophysics, Atmosphere, and Solar Wind Environment*, p. 259.
- Bougher, S.W., Brecht, A.S., Schulte, R., Fischer, J., Parkinson, C.D., Mahieux, A., Wilquet, V., Vandaele, A., 2015. Upper atmosphere temperature structure at the venusian terminators: a comparison of SOIR and VTGCM results. *Planet Sp. Sci.* 113, 336–346. doi:10.1016/j.pss.2015.01.012.
- Bougher, S.W., Rafkin, S., Drossart, P., 2006. Dynamics of the venus upper atmosphere: outstanding problems and new constraints expected from venus express. *Planet Sp. Sci.* 54, 1371–1380. doi:10.1016/j.pss.2006.04.023.
- Bougher, S.W., Roble, R.G.E., Dickinson, R.E., Ridley, E.C., 1988. Venus mesosphere and thermosphere. III - three-dimensional general circulation with coupled dynamics and composition. *Icarus* 73, 545–573. doi:10.1016/0019-1035(88)90064-4.
- Brecht, A.S., Bougher, S.W., 2012. Dayside thermal structure of venus' upper atmosphere characterized by a global model. *J. Geophys. Res. (Planets)* 117, 8002. doi:10.1029/2012JE004079.
- Brecht, A.S., Bougher, S.W., Gérard, J.C., Parkinson, C.D., Rafkin, S., Foster, B., 2011. Understanding the variability of nightside temperatures, NO UV and O_2 IR nightglow emissions in the venus upper atmosphere. *J. Geophys. Res. (Planets)* 116, 8004. doi:10.1029/2010JE003770.
- Brecht, A.S., Bougher, S.W., Gérard, J.C., Soret, L., 2012. Atomic oxygen distributions in the venus thermosphere: comparisons between venus express observations and global model simulations. *Icarus* 217, 759–766. doi:10.1016/j.icarus.2011.06.033.
- Chaufray, J.Y., Bertaux, J.L., Leblanc, F., 2012. First observation of the venus UV dayglow at limb from SPICAV/VEX. *Geophys. Res. Lett.* 39, 20201. doi:10.1029/2012GL036266.
- Chaufray, J.Y., González-Galindo, F., Forget, F., López-Valverde, M.A., Leblanc, F., Modolo, R., Hess, S., 2015. Variability of the hydrogen in the martian upper atmosphere as simulated by a 3d atmosphere-exosphere coupling. *Icarus* 245, 282–294. doi:10.1016/j.icarus.2014.08.038.
- Clancy, R.T., Muhleman, D.O., 1985. Diurnal CO variations in the venus mesosphere from CO microwave spectra. *Icarus* 64, 157–182. doi:10.1016/0019-1035(85)90084-3.
- Clancy, R.T., Sandor, B.J., Moriarty-Schieven, G., 2012. Thermal structure and CO distribution for the venus mesosphere/lower thermosphere: 2001–2009 inferior conjunction sub-millimeter CO absorption line observations. *Icarus* 217, 779–793. doi:10.1016/j.icarus.2011.05.032.
- Crisp, D., 1986. Radiative forcing of the venus mesosphere. i - solar fluxes and heating rates. *Icarus* 67, 484–514. doi:10.1016/0019-1035(86)90126-0.
- Encrenaz, T., Greathouse, T., Richter, M., DeWitt, C., Widemann, T., Bézard, B., Fouchet, T., Atreya, S., Sagawa, H., 2016. Imaging spectroscopy of venus in the thermal infrared: variability of HDO and SO₂, and daily variations of the thermal structure. In: *EGU General Assembly Conference Abstracts*, p. 2484.
- Eymet, V., Fournier, R., Dufresne, J.L., Lebonnois, S., Hourdin, F., Bullock, M.A., 2009. Net exchange parameterization of thermal infrared radiative transfer in venus' atmosphere. *J. Geophys. Res. (Planets)* 114, 11008. doi:10.1029/2008JE003276.
- Feofilov, A.G., Kutepov, A.A., 2012. Infrared radiation in the mesosphere and lower thermosphere: energetic effects and remote sensing. *Surv. Geophys.* 33, 1231–1280. doi:10.1007/s10712-012-9204-0.
- Forget, F., Hourdin, F., Fournier, R., Hourdin, C., Talagrand, O., Collins, M., Lewis, S.R., Read, P.L., Huot, J.P., 1999. Improved general circulation models of the Martian atmosphere from the surface to above 80 km. *J. Geophys. Res.* 104, 24,155–24,176.
- Fox, J.L., 1988. Heating efficiencies in the thermosphere of Venus reconsidered. *Planet Space Sci.* 36, 37–46. doi:10.1016/0032-0633(88)90144-4.
- Fox, J.L., Bougher, S.W., 1991. Structure, luminosity, and dynamics of the venus thermosphere. *Sp. Sci. Rev.* 55, 357–489. doi:10.1007/BF00177141.
- Garcia, R., Drossard, P., Piccioni, G., Lopez-Valverde, M., Occhipinti, G., 2009. Gravity waves in the upper atmosphere of venus revealed by CO₂ nonlocal thermodynamic equilibrium emissions. *J. Geophys. Res.* 114, E00B32. doi:10.1029/2008JE003073.
- Gérard, J.C., Saglam, A., Piccioni, G., Drossart, P., Montmessin, F., Bertaux, J.L., 2009. Atomic oxygen distribution in the venus mesosphere from observations of O_2 infrared airglow by VIRTIS-venus express. *Icarus* 199, 264–272. doi:10.1016/j.icarus.2008.09.016.
- Gérard, J.C., Soret, L., Migliorini, A., Piccioni, G., 2013. Oxygen nightglow emissions of venus: vertical distribution and collisional quenching. *Icarus* 223, 602–608. doi:10.1016/j.icarus.2012.11.019.
- Gérard, J.C., Soret, L., Piccioni, G., Drossart, P., 2014. Latitudinal structure of the venus O_2 infrared airglow: a signature of small-scale dynamical processes in the upper atmosphere. *Icarus* 236, 92–103. doi:10.1016/j.icarus.2014.03.028.
- Gilli, G., López-Valverde, M.A., Drossart, P., Piccioni, G., Erard, S., Cardesin Moineau, A., 2009. Limb observations of CO₂ and CO non-LTE emissions in the venus atmosphere by VIRTIS/venus express. *J. Geophys. Res. (Planets)* 114, 0–+. doi:10.1029/2008JE003112.
- Gilli, G., López-Valverde, M.A., Funke, B., López-Puertas, M., Drossart, P., Piccioni, G., Formisano, V., 2011. Non-LTE CO limb emission at 4.7 μ m in the upper atmosphere of venus, mars and earth: observations and modeling. *Planet Sp. Sci.* 59, 1010–1018. doi:10.1016/j.pss.2010.07.023.
- Gilli, G., López-Valverde, M.A., Peralta, J., Bougher, S., Brecht, A., Drossart, P., Piccioni, G., 2015. Carbon monoxide and temperature in the upper atmosphere of venus from VIRTIS/venus express non-LTE limb measurements. *Icarus* 248, 478–498. doi:10.1016/j.icarus.2014.10.047.
- González-Galindo, F., Chaufray, J.Y., López-Valverde, M.A., Gilli, G., Forget, F., Leblanc, F., Modolo, R., Hess, S., Yagi, M., 2013. Three-dimensional martian ionosphere model: I. the photochemical ionosphere below 180 km. *J. Geophys. Res. (Planets)* 118, 2105–2123. doi:10.1002/jgre.20150.
- González-Galindo, F., Forget, F., López-Valverde, M.A., Angelats i Coll, M., 2009. A ground-to-exosphere martian general circulation model: 2. atmosphere during solstice conditions. thermospheric polar warming. *J. Geophys. Res. (Planets)* 114, 8004–+. doi:10.1029/2008JE003277.
- González-Galindo, F., López-Valverde, M.A., Angelats i Coll, M., Forget, F., 2005. Extension of a martian general circulation model to thermospheric altitudes: UV heating and photochemical models. *J. Geophys. Res. (Planets)* 110, 9008–+. doi:10.1029/2004JE002553.
- Grassi, D., Migliorini, A., Montabone, L., Lebonnois, S., Cardesin-Moineau, A., Piccioni, G., Drossart, P., Zasova, L.V., 2010. Thermal structure of venusian nighttime mesosphere as observed by VIRTIS-venus express. *J. Geophys. Res. (Planets)* 115, 9007. doi:10.1029/2009JE003553.
- Grassi, D., Politi, R., Ignatiev, N.I., Plainaki, C., Lebonnois, S., Wolkenberg, P., Montabone, L., Migliorini, A., Piccioni, G., Drossart, P., 2014. The venus nighttime atmosphere as observed by the VIRTIS-m instrument. average fields from the complete infrared data set. *J. Geophys. Res. (Planets)* 119, 837–849. doi:10.1002/2013JE004586.
- Guilbon, S., Määttänen, A., Montmessin, F., 2015. Modeling venus' clouds with the moment method: paving the way for 3d GCM simulations. *European Planetary Science Congress 2015, Held 27 September - 2 October, 2015 in Nantes, France, EPSC2015-614*, 10.
- Gurwell, M.A., Muhleman, D.O., Shah, K.P., Berge, G.L., Rudy, D.J., Grossman, A.W., 1995. Observations of the CO bulge on venus and implications for mesospheric winds. *Icarus* 115, 141–158. doi:10.1006/icar.1995.1085.
- Haus, R., Kappel, D., Arnold, G., 2013. Self-consistent retrieval of temperature profiles and cloud structure in the northern hemisphere of venus using VIRTIS/VEX and PMV/VENERA-15 radiation measurements. *Planet Sp. Sci.* 89, 77–101. doi:10.1016/j.pss.2013.09.020.
- Haus, R., Kappel, D., Arnold, G., 2014. Atmospheric thermal structure and cloud features in the southern hemisphere of venus as retrieved from VIRTIS/VEX radiation measurements. *Icarus* 232, 232–248. doi:10.1016/j.icarus.2014.01.020.
- Hedin, A.E., Niemann, H.B., Kasprzak, W.T., Seiff, A., 1983. Global empirical model of the venus thermosphere. *J. Geophys. Res.* 88, 73–83. doi:10.1029/JA088iA01p00073.
- Hoshino, N., Fujiwara, H., Takagi, M., Kasaba, Y., 2013. Effects of gravity waves on the day-night difference of the general circulation in the venusian lower thermosphere. *J. Geophys. Res. (Planets)* 118, 2004–2015. doi:10.1002/jgre.20154.

- Hourdin, F., Couvreur, F., Menut, L., 2002. Parameterization of the dry convective boundary layer based on a mass flux representation of thermals. *J. Atmosph. Sci.* 59, 1105–1123. doi:10.1175/1520-0469(2002)059<1105:POTDCB>2.0.CO;2.
- Hourdin, F., Musat, I., Bony, S., Braconnot, P., Codron, F., Dufresne, J.L., Fairhead, L., Filiberti, M.A., Friedlingstein, P., Grandpeix, J.Y., Krinner, G., Levan, P., Li, Z.X., Lott, F., 2006. The LMDZ4 general circulation model: climate performance and sensitivity to parametrized physics with emphasis on tropical convection. *Climate Dyn.* 27, 787–813. doi:10.1007/s00382-006-0158-0.
- Huestis, D.L., Bougher, S.W., Fox, J.L., Galand, M., Johnson, R.E., Moses, J.I., Pickering, J.C., 2008. Cross sections and reaction rates for comparative planetary aeronomy. *Sp. Sci. Rev.* 139, 63–105. doi:10.1007/s11214-008-9383-7.
- Kasprzak, W.T., Niemann, H.B., Hedin, A.E., Bougher, S.W., Hunten, D.M., 1993. Neutral composition measurements by the pioneer venus neutral mass spectrometer during orbiter re-entry. *Geophys. Res. Lett.* 20, 2747–2750. doi:10.1029/93GL02241.
- Keating, G.M., Bertaux, J.L., Bougher, S.W., Dickinson, R.E., Cravens, T.E., Hedin, A.E., 1985. Models of venus neutral upper atmosphere - structure and composition. *Adv. Sp. Res.* 5, 117–171. doi:10.1016/0273-1177(85)90200-5.
- Keating, G.M., Nicholson, J.Y., Lake, L.R., 1980. Venus upper atmosphere structure. *J. Geophys. Res.* 85, 7941–7956. doi:10.1029/JA085iA13p07941.
- Knollenberg, R., Hunten, D., 1980. The microphysics of the clouds of Venus: results of the pioneer venus particle size spectrometer experiment. *J. Geophys. Res.* 85, 8039–8058.
- Krasnopolsky, V.A., 2012. A photochemical model for the venus atmosphere at 47–112 km. *Icarus* 218, 230–246. doi:10.1016/j.icarus.2011.11.012.
- Krause, P., Sornig, M., Wischniewski, C., Herrmann, M., Stangier, T., Sonnabend, G., Kostiuk, T., Livengood, T., 2015. Long-term variation of temperature and dynamic at the morning terminator in venus upper atmosphere from ground-based infrared heterodyne spectroscopy. In: *European Planetary Science Congress 2015*, held 27 September - 2 October, 2015 in Nantes, France, 10, pp. EPSC2015-544.
- Krause, P., Wischniewski, C., Sornig, M., Stangier, T., Sonnabend, G., Herrmann, M., Wiegand, M., Kostiuk, T., Livengood, T., 2016. Temperature measurements in venus upper atmosphere between 2007 and 2015 from ground-based infrared heterodyne spectroscopy. In: *EGU General Assembly Conference Abstracts*, p. 16468.
- Lebonnois, S., Covey, C., Grossman, A., Parish, H., Schubert, G., Walterscheid, R., Lauritzen, P., Jablonowski, C., 2012. Angular momentum budget in general circulation models of superrotating atmospheres: a critical diagnostic. *J. Geophys. Res. (Planets)* 117, 12004. doi:10.1029/2012JE004223.
- Lebonnois, S., Hourdin, F., Eymet, V., Crespin, A., Fournier, R., Forget, F., 2010. Superrotation of venus' atmosphere analyzed with a full general circulation model. *J. Geophys. Res. (Planets)* 115, 6006. doi:10.1029/2009JE003458.
- Lebonnois, S., Sugimoto, N., Gilli, G., 2016. Wave analysis in the atmosphere of venus below 100-km altitude, simulated by the LMD venus GCM. *Icarus* 278, 38–51. doi:10.1016/j.icarus.2016.06.004.
- Lefèvre, F., Bertaux, J.L., Clancy, R.T., Encrenaz, T., Fast, K., Forget, F., Lebonnois, S., Montmessin, F., Perrier, S., 2008. Heterogeneous chemistry in the atmosphere of mars. *Nature* 454, 971–975. doi:10.1038/nature07116.
- Lefèvre, F., Lebonnois, S., Montmessin, F., Forget, F., 2004. Three-dimensional modeling of ozone on mars. *J. Geophys. Res.* 109, E07004. doi:10.1029/2004JE002268.
- Lefèvre, M., Spiga, A., Lebonnois, S., 2016. Three-dimensional mesoscale modeling of the venusian cloud layer and associated gravity waves. Submitted to JGR.
- Lellouch, E., Clancy, T., Crisp, D., Kliore, A.J., Titov, D., Bougher, S.W., 1997. Monitoring of mesospheric structure and dynamics. In: Bougher, S.W., Hunten, D.M., Phillips, R.J. (Eds.), *Venus II: Geology, Geophysics, Atmosphere, and Solar Wind Environment*, p. 295.
- Limaye, S.S., Bougher, S., Chamberlain, S., Clancy, R.T., Gilli, G., Grassi, D., Haus, R., Herrmann, M., Imamura, T., Kohler, E., Krause, P., Lebonnois, S., Mahieux, A., Sandor, A., Sornig, M., Svedhem, H., Tellmann, S., Vandaele, A.C., Widemann, T., Wilson, C., Mueller-Wodarg, I., Zasova, L., 2015. Improved knowledge of venus atmospheric structure. In: *European Planetary Science Congress 2015*, held 27 September - 2 October, 2015 in Nantes, France, 10, pp. EPSC2015-758.
- Lopez-Puertas, M., Taylor, F.W., 2001. Non-LTE Radiative Transfer in the Atmosphere. *World Scientific Pub.*, Singapore, Series on Atmospheric Oceanic and Planetary Physics, vol. 3 ISBN 9810245661.
- Lopez-Valverde, M.A., Lopez-Puertas, M., 1994. A non-local thermodynamic equilibrium radiative transfer model for infrared emission in the atmosphere of mars. 2: daytime populations of vibrational levels. *J. Geophys. Res.* 99, 13117–13132. doi:10.1029/94JE01091.
- López-Valverde, M.A., López-Puertas, M., Funke, B., Gilli, G., García-Comas, M., Drossart, P., Piccioni, G., Formisano, V., 2011. Modelling the atmospheric limb emission of CO₂ at 4.3 μm in the terrestrial planets. *Planet. Space Sci.* 59, 988–998. doi:10.1016/j.pss.2010.02.001.
- Lott, F., Guez, L., 2013. A stochastic parameterization of the gravity waves due to convection and its impact on the equatorial stratosphere. *J. Geophys. Res. (Atmosph.)* 118, 8897–8909. doi:10.1002/jgrd.50705.
- Määttänen, A., Guilbon, S., Stolzenbach, A., Bekki, S., Montmessin, F., 2015. VenLA: the LATMOS venus cloud model. In: *European Planetary Science Congress 2015*, held 27 September - 2 October, 2015 in Nantes, France, 10, pp. EPSC2015-634.
- Madronich, S., Flocke, S., 1999. The role of solar radiation in atmospheric chemistry. In: *Environmental Photochemistry*. Springer, pp. 1–26.
- Mahieux, A., Vandaele, A.C., Bougher, S.W., Drummond, R., Robert, S., Wilquet, V., Chamberlain, S., Piccialli, A., Montmessin, F., Tellmann, S., Pätzold, M., Häusler, B., Bertaux, J.L., 2015. Update of the venus density and temperature profiles at high altitude measured by SOIR on board venus express. *Planet Sp. Sci.* 113, 309–320. doi:10.1016/j.pss.2015.02.002.
- Mellor, G.L., Yamada, T., 1982. Development of a turbulent closure model for geophysical fluid problems. *Rev. Geophys. Space Phys.* 20, 851–875.
- Migliorini, A., Grassi, D., Montabone, L., Lebonnois, S., Drossart, P., Piccioni, G., 2012. Investigation of air temperature on the nightside of venus derived from VIRTIS-h on board venus-express. *Icarus* 217, 640–647. doi:10.1016/j.icarus.2011.07.013.
- Niemann, H.B., Kasprzak, W.T., Hedin, A.E., Hunten, D.M., Spencer, N.W., 1980. Mass spectrometric measurements of the neutral gas composition of the thermosphere and exosphere of venus. *J. Geophys. Res.* 85, 7817–7827. doi:10.1029/JA085iA13p07817.
- Peralta, J., Hueso, R., Sánchez-Lavega, A., Piccioni, G., Lanciano, O., Drossart, P., 2008. Characterization of mesoscale gravity waves in the upper and lower clouds of venus from VEX-VIRTIS images. *J. Geophys. Res. (Planets)* 113, 0. doi:10.1029/2008JE003185.
- Peralta, J., López-Valverde, M.A., Gilli, G., Piccialli, A., 2016. Dayside temperatures in the venus upper atmosphere from venus express/VIRTIS nadir measurements at 4.3 μm. *A & A* 585, A53. doi:10.1051/0004-6361/201527191.
- Piccialli, A., Montmessin, F., Belyaev, D., Mahieux, A., Marcq, E., Bertaux, J.L., Tellmann, S., Vandaele, A.C., Korablev, O., 2015. Thermal structure of venus nightside upper atmosphere measured by stellar occultations with SPI-CAV/venus express. *Planet Sp. Sci.* 113, 321–335. doi:10.1016/j.pss.2014.12.009.
- Piccialli, A., Titov, D.V., Sanchez-Lavega, A., Peralta, J., Shalygina, O., Markiewicz, W.J., Svedhem, H., 2014. High latitude gravity waves at the venus cloud tops as observed by the venus monitoring camera on board venus express. *Icarus* 227, 94–111. doi:10.1016/j.icarus.2013.09.012.
- Roldán, C., López-Valverde, M.A., López-Puertas, M., Edwards, D.P., 2000. Non-LTE infrared emissions of CO₂ in the atmosphere of venus. *Icarus* 147, 11–25. doi:10.1006/icar.2000.6432.
- Sander, S.P., Abbott, J., Barker, J., Burkholder, J., Friedl, R., Golden, D., 2011. *Chemical Kinetics and Photochemical Data for Use in Atmospheric Studies*, Evaluation No. 17. Technical Report. JPL.
- Schubert, G., Covey, C., del Genio, A., Elson, L.S., Keating, G., Seiff, A., Young, R.E., Apt, J., Counselman, C.C., Kliore, A.J., Limaye, S.S., Revercomb, H.E., Sromovsky, L.A., Suomi, V.E., Taylor, F., Woo, R., von Zahn, U., 1980. Structure and circulation of the venus atmosphere. *J. Geophys. Res.* 85, 8007–8025. doi:10.1029/JA085iA13p08007.
- Seiff, A., 1983. Thermal structure of the atmosphere of venus 215–279.
- Sharma, R.D., 2014. Technical note: a new mechanism of 15 μm emission in the mesosphere-lower thermosphere (MLT). *Atmosph. Chem. Phys. Discuss.* 14, 25083–25093. doi:10.5194/acpd-14-25083-2014.
- Sharma, R.D., Wintersteiner, P.P., 1990. Role of carbon dioxide in cooling planetary thermospheres. *Geophys. Res. Lett.* 17, 2201–2204.
- Sonnabend, G., Kroetz, P., Sornig, M., Stupar, D., 2010. Direct observations of venus upper mesospheric temperatures from ground based spectroscopy of CO₂. *Geophys. Res. Lett.* 37, L11102. doi:10.1029/2010GL043335.
- Soret, L., Gérard, J.C., Montmessin, F., Piccioni, G., Drossart, P., Bertaux, J.L., 2012. Atomic oxygen on the venus nightside: global distribution deduced from airglow mapping. *Icarus* 217, 849–855. doi:10.1016/j.icarus.2011.03.034.
- Soret, L., Gérard, J.C., Piccioni, G., Drossart, P., 2014. Time variations of O₂(a¹Δ) nightglow spots on the venus nightside and dynamics of the upper mesosphere. *Icarus* 237, 306–314. doi:10.1016/j.icarus.2014.03.034.
- Stolzenbach, A., Lefèvre, F., Lebonnois, S., Määttänen, A., Bekki, S., 2014. Three-dimensional modelling of venus photochemistry. In: *EGU General Assembly Conference Abstracts*, p. 5315.
- Stolzenbach, A., Lefèvre, F., Lebonnois, S., Määttänen, A.E., Bekki, S., 2015. Three-dimensional modelling of venus photochemistry. *AGU Fall Meeting Abs.*
- Svedhem, H., Müller-Wodarg, I., 2014. Results of the venus express aerobraking campaign. In: *AAS/Division for Planetary Sciences Meeting Abstracts*, p. 302.09.
- Svedhem, H., Wilson, C., Piccioni, G., 2015. Introduction to the special issue on venus exploration. *Planet Sp. Sci.* 113, 1. doi:10.1016/j.pss.2015.06.003.
- Tellmann, S., Häusler, B., Hinson, D.P., Tyler, G.L., Andert, T.P., Bird, M.K., Imamura, T., Pätzold, M., Remus, S., 2012. Small-scale temperature fluctuations seen by the vera radio science experiment on venus express. *Icarus* 221, 471–480. doi:10.1016/j.icarus.2012.08.023.
- Tellmann, S., Pätzold, M., Häusler, B., Bird, M.K., Tyler, G.L., 2009. Structure of the venus neutral atmosphere as observed by the radio science experiment vera on venus express. *J. Geophys. Res. (Planets)* 114, E00B36. doi:10.1029/2008JE003204.
- Vandaele, A.C., Chamberlain, S., Mahieux, A., Ristic, B., Robert, S., Thomas, I., Trompet, L., Wilquet, V., Belyaev, D., Fedorova, A., Korablev, O., Bertaux, J.L., 2016. Contribution from SOIR/VEX to the updated venus international reference atmosphere (VIRA). *Adv. Sp. Res.* 57, 443–458. doi:10.1016/j.asr.2015.08.012.
- Wischniewski, C., Sornig, M., Sonnabend, G., Stangier, T., Krause, P., Herrmann, M., Kostiuk, T., Livengood, T., 2015. Thermal structure of venus' dayside in 110 km altitude based on ground-based heterodyne observations between 2007 and 2014. In: *European Planetary Science Congress 2015*, held 27 September - 2 October, 2015 in Nantes, France, 10, pp. EPSC2015-546.
- Woo, R., Armstrong, J.W., Ishimaru, A., 1980. Radio occultation measurements of turbulence in the venus atmosphere by pioneer venus. *J. Geophys. Res.* 85, 8031–8038. doi:10.1029/JA085iA13p08031.
- Zalucha, A.M., Brecht, A.S., Rafkin, S., Bougher, S.W., Alexander, M.J., 2013. Incorporation of a gravity wave momentum deposition parameterization into the venus thermosphere general circulation model (VTGCM). *J. Geophys. Res. (Planets)* 118, 147–160. doi:10.1029/2012JE004168.
- Zhang, S., Bougher, S.W., Alexander, M.J., 1996. The impact of gravity waves on the venus thermosphere and O₂ IR nightglow. *J. Geophys. Res.* 101, 23195–23206. doi:10.1029/96JE02035.